Bubble formation in helium-implanted nanostructured 14YWT and CNA ferritic alloys at elevated temperatures

Yan-Ru Lin[1*], Wei-Ying Chen[2], Lizhen Tan[3], David T. Hoelzer[3], Zhanfeng Yan[4], Cheng-Yu Hsieh[5], Chun-Wei Huang[5], Steven John Zinkle[1, 3, 6]

[1]*Department of Material Science and Engineering, University of Tennessee, Knoxville, TN 37996, USA*

[2]*Nuclear Science and Engineering Division, Argonne National Laboratory, Argonne, IL 60439, USA*

[3]*Materials Science and Technology Division, Oak Ridge National Laboratory, Oak Ridge, TN 37831, USA*

[4]*State Key Laboratory of Nuclear Physics and Technology, Center for Applied Physics and Technology, Peking University, Beijing, 100871, China*

[5]*Material and Chemical Research Laboratories, Industrial Technology Research Institute, Hsinchu 31040, Taiwan*

[6]*Department of Nuclear Engineering, University of Tennessee, Knoxville, TN 37996, USA*

*Corresponding author

Postal Address: 414 Ferris Hall, 1508 Middle Drive, Knoxville, TN 37996, USA

Email: ylin52@vols.utk.edu

Co-author email addresses in order of appearance:

wychen@anl.gov

tanl@ornl.gov

hoelzerd@ornl.gov

zhanfengyan@pku.edu.cn

cyhsieh@itri.org.tw

chunwei1220@gmail.com

szinkle@utk.edu

Abstract

Helium bubble formation was examined by scanning/transmission electron microscopy (S/TEM) in Fe-9/10Cr binary alloys and two dispersion strengthened nanostructured alloys (CNA3 and 14YWT) after ex-situ and in-situ He implantation to ~10,000 appm at 500 to 900 °C. The combination of high-resolution STEM images and electron energy loss spectroscopy (EELS) revealed that the Y-Ti-O nanoclusters in 14YWT were distributed the most uniform and exhibited a one-to-one relationship for bubble attachment to the nanoclusters. In the in-situ experiment at 900 °C, grain boundary cracking was severe in the Fe-10Cr model alloy, but not in the nanostructured alloys. From 500-900 °C, the bubble size generally increased with increasing irradiation temperature, while the bubble density decreased with increasing temperature. At the same temperatures, the cavity size in the implanted materials was in the order of Fe-9/10Cr > CNA3 > 14YWT, while the cavity density showed the opposite order. The observed bubble number densities for the nanostructured alloys are comparable to the nanoparticle density, suggesting that the nanoparticles in both alloys were effective in trapping He. Our results indicate that very high He concentrations can be managed in nanostructured alloys by sequestering the helium into smaller bubbles (which leads to a lower volume swelling value) and to shield He from the grain boundaries. This can be attributed to the much higher sink strength associated with the nanoclusters or the He trapping ability between different types of nanoclusters.

Keywords: nanostructured ferritic alloy, ODS alloy; *in-situ* TEM; radiation effects; helium bubble

Graphic abstract

1 Introduction

Structural materials in nuclear fission and fusion reactors have to withstand high temperature, neutron irradiation damage, and helium generated by (n,α) transmutation reactions. The synergistic effect of He along with radiation damage can cause unwanted degradation of the mechanical performance of structural materials and impact the safety of nuclear reactors [1, 2]. Helium in irradiated materials can cause low-temperature hardening [3], cavity swelling [4, 5], and high-temperature grain boundary embrittlement [6]; they ultimately determine the operating temperature and dose limits for most materials. It has been proposed that these effects could be mitigated by increasing the number of He trapping sites to control the bubble size or to shield He from the grain boundaries [7, 8]. The trapping sites for radiation-induced vacancies, interstitials, and He atoms are so-called sink strength. This concept has led to the development of nanostructured ferritic alloys (NFAs) [8], with engineered high-sink-strength microstructures, such as castable nanostructured alloys (CNAs) [9] or Oxide dispersion-strengthened (ODS) steels [10-12]. Several studies have shown that nano-scale dispersoids, that are stable under prolonged high temperature neutron service, can enhance mechanical properties, improve the radiation resistance of the material, and sequester large amounts of helium into small bubbles based on the concept of high sink strength [13-18]. However, there is still a lack of systematic irradiation data showing how the density of nanoparticles and their He trapping ability (binding energy) in advanced ferritic alloys affect the helium bubble density and size at elevated temperatures.

By a pressure effect, helium stabilizes cavity formation at different formation sites (e.g. grain matrices, dislocations, precipitate interfaces, and grain boundaries) [8]. Here, a cavity is a vacancy cluster that may or may not contain gas impurities, while a He bubble is a pressurized cavity that contains helium. Prior studies [5, 19, 20] have shown that when the He concentration is low, the cavity swelling initially increases with increasing He concentration. Conversely, at very high He concentrations, the cavity swelling decreases with increasing He concentration. As for the effect of temperature, in general, the bubble formation at a lower temperature is diffusion controlled, while at higher temperatures it is generally dominated by the thermal dissociation rate of vacancies from helium-filled cavities [21]. Besides, prior studies have shown that hot-implanted and cold-implanted helium (followed by annealing process) would result in a different bubble density [19, 21]. In general, hot-implanted helium experiments are more favorable to simulate the transmutant He in reactor irradiation conditions.

As a reference for studying fundamental radiation damage mechanisms in advanced ferritic/martensitic (F/M) alloys, several Fe-Cr model alloy investigations have been conducted to understand helium effects [22-25]. In general, the cavity size increases and the density decreases with increasing irradiation temperature (cavity coarsening) [24]. At higher irradiation temperatures (>550 °C), the formation of non-spherical faceted cavities was often observed [23, 24]. Yan et al. reported a spatial distribution change (from homogeneous to heterogeneous) of bubbles in He irradiated Fe-9Cr (wt%) alloys at elevated temperatures [24]. Their result showed heterogeneous nucleation of bubbles at dislocations at temperatures above 700 °C, and distinct activation energies for helium at different temperatures. For the Cr solution effect, a study comparing Fe-9Cr to pure Fe by Ono et al. [22] suggested lower bubble mobility in He implanted Fe-9Cr, which could be caused by Cr segregation on the bubble surface.

Although the formation of He bubbles in binary Fe-Cr alloys have been widely studied, and advanced manufacturing techniques are enabling fabrication of high-performance structural alloys with finely-dispersed nanoclusters to achieve high sink strengths, relatively fewer studies of the effects of the nanoparticles on the formation of helium bubbles have been published. Therefore, the objective of this research is to study the bubble size and density in two advanced nanostructured F/M alloys (CNA3 and 14YWT) with different precipitate features and different initial dispersoid sink strengths. Coordinated ex-situ bulk material irradiation experiments with post-irradiation examinations and in-situ ion irradiation on transmission electron microscopy (TEM) samples were conducted to provide a better understanding of the formation of He bubbles in nanostructured Fe-Cr alloys. In this study, cavity formation in high purity Fe-9/10Cr, CNA3, and 14YWT materials with ex-situ and in-situ He implantation (to ~10,000 appm at 500 to 900°C) was examined by TEM. In addition, the 600°C in-situ irradiated samples were annealed to 900 °C to compare with the 900°C directly hot implanted experiments.

2 Experimental

2.1 Materials

14YWT-SM10 and CNA3 advanced F/M steels, and model Fe-9/10Cr (wt%) alloys were used in this study. The TEM images and typical compositions of the as-received materials are given in Fig. A.1 and Table A.1, respectively. The castable nanostructured alloys (CNAs) with fine MX-type (M=Ti/Ta/V, X=C/N) nanoparticles and coarse $M_{23}C_6$ particles were developed at Oak Ridge National Laboratory (ORNL) [9]. The fine particle density and average diameter in the CNA3 alloy were around 10^{21}-10^{22} m^{-3} and 3-20 nm, respectively. On the other hand, the

coarse $M_{23}C_6$ particles have an average diameter greater than ~70 nm, with a lower density on the order of 10^{18}–10^{19} m^{-3}. The prior-austenite grain size was near 10-60 μm. The dislocation density of the as-fabricated CNA3 alloy was ~3×10^{14} m^{-2}. The 14YWT alloy is an ODS alloy [12]. The SM10 heat of 14YWT demonstrated a uniquely fine and uniform microstructure of nanograin structure (grain size ~0.2 μm) and high density (~10^{24} m^{-3}) of Y-Ti-O nanoparticles (diameter about 2-3 nm). Other particles, such as $Y_2Ti_2O_7$, TiN, or TiC, with a relatively larger size of 5-30 nm were also observed in 14YWT. The dislocation density of the as-fabricated 14YWT alloy was ~2×10^{14} m^{-2}. Fe-10Cr had very low impurities, whereas Fe-9Cr included 0.1-0.6 wt% of Mn, Mo, Si, V, and W. Both binary alloys were heat-treated to reduce dislocation density. The average grain size of the Fe-9Cr and Fe-10Cr alloys are ~0.6 and 82 μm, respectively. The fabrication process of the Fe-9/10Cr model alloys are described elsewhere [24, 26].

2.2 Ex-situ He-implantation in bulk materials

The 275 keV He implantation experiments on the Fe-10Cr model alloy and the NFAs (CNA3 and 14YWT) were carried out at 500 and 700 °C with the High Voltage Engineering Europe (HVEE) implanter at National Tsing Hua University in Taiwan. Bulk materials were cut into 2 mm× 2 mm square specimens by a low-speed diamond saw. After cutting, the bar specimens were mechanically polished using sandpaper up to 2000 grit and polishing fluids with particles down to 0.01 μm. The final thickness of the square samples was about 0.5 μm. Fig. 1a shows the overall holder and sample arrangement. The 2 mm×2 mm samples were attached on a 3 mm×15 mm Fe strip with silver paste. The strips were then placed into a groove on a

Molybdenum holder. Quartz plates were placed on the periphery of the target holder (next to the Fe alloy specimens) to confirm the ion beam profile and position. Also, thermocouple wires were welded on the samples to measure the temperature during irradiation. The fluence and peak helium concentration were 1.28×10^{20} m^{-3} and ~8,000 appm, respectively. Fig. 1b shows the depth profile of the He concentration calculated by the Stopping and Range of Ions in Matter (SRIM-2013) program using the "quick calculation" vacancy.text files with displacement energy, E_d=40 eV for Fe target. The peak He production rate at depth 0.6 μm was 2.4 appm He/sec. In addition, the dose and dose rate at depth 0.6 μm was 0.3 dpa and 2.8×10^{-5} dpa/s, respectively. The irradiated samples were prepared for TEM and STEM analysis using a focused ion beam (FIB) in a cross beam Zeiss Auriga FIB/SEM. A gallium FIB beam probe at 2 keV was used for the final polishing to minimize FIB beam damage.

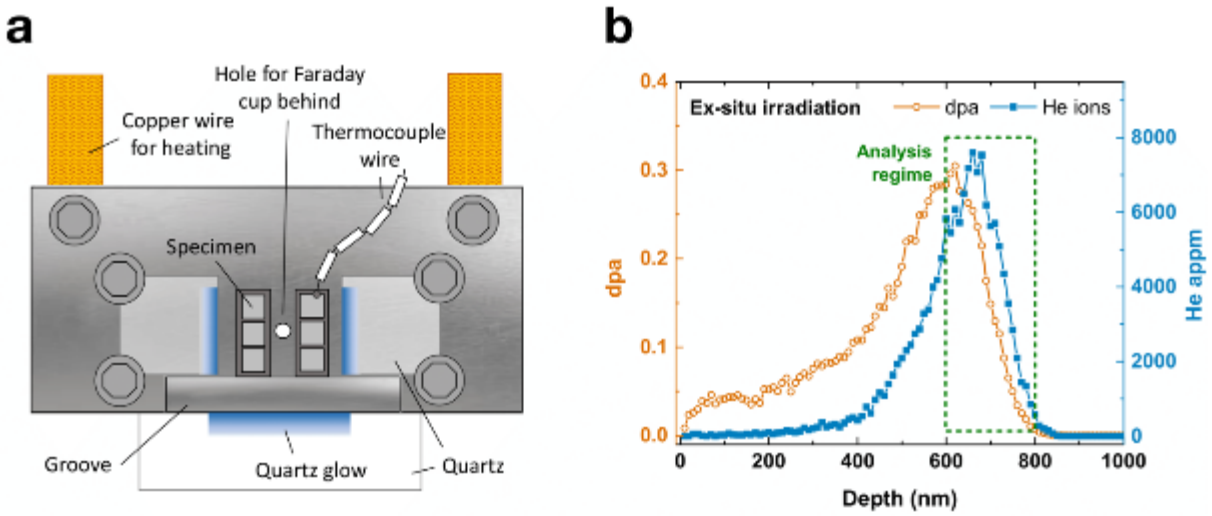

Fig. 1. (a) Sample loading and arrangement for the bulk material ex-situ irradiation; (b) SRIM simulation for 275 keV He ions in Fe target (E_d=40 eV) with a total fluence of 1.28×10^{20} m^{-2}.

2.3 In-situ He-implantation in thin foil materials

For the *in-situ* study, the samples were cut into 3-mm disks for transmission electron microscopy (TEM) via wire electrical discharge machining (EDM) and mechanically thinned from both sides to ~150 μm thick before electropolishing. The thinned disks were then electrochemically polished in a Struers Tenupol 5 electropolisher using a mixed solution of 5 vol% perchloric acid and 95 vol% methanol at -40 °C under an applied voltage of 23-27 V. Following perforation, rinsing was performed in methanol for two minutes. After twin-jet electropolishing, the electron-transparent region near the perforated hole of the wedge-shaped TEM samples was investigated.

The TEM thin foils of Fe-10Cr, CNA3, and 14YWT materials were irradiated with 10 keV single He ion beam, with a 15° incident angle, at 600 and 900 °C. The thin TEM foils were irradiated at the Intermediate-Voltage Electron Microscopy (IVEM)-Tandem facility in Argonne National Laboratory (ANL) (Fig. 2a). As shown in Fig. 2b, with a total fluence near 6.82×10^{19} m^{-2}, based on the SRIM-2013 calculation (also by "QC-vacancy.txt" method and E_d=40 eV), the peak radiation damage and He concentration at depth 60 nm were roughly 0.3 dpa and 12,000 appm, respectively. For the 600°C in-situ irradiated samples, when the peak dose reached 12,000 appm, we stopped the implantation and subsequently performed post-irradiation annealing to 900 °C. The annealing results were used to compare with the 900°C directly-hot-implanted experiments. Table 1. summarizes the irradiation condition of both the ex-situ bulk material and in-situ thin foil studies.

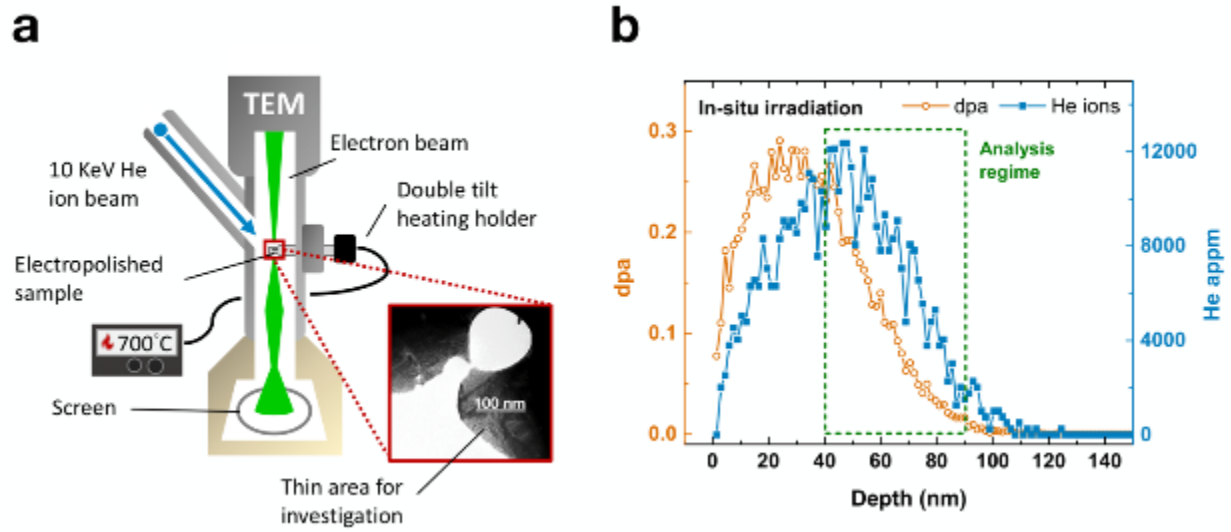

Fig. 2. (a) Schematic diagram of the in-situ irradiation experiment; (b) SRIM simulation for 10 keV He ions in Fe target (E_d=40 eV) with total fluence of 6.82×10^{19} m^{-2}

Table 1. Conditions of helium implantations.

Sample type	Ion Species	Material	Temperature (°C)	Fluence (m^{-2})	Peak He concentration (appm)	Irradiation time (sec)
Thin foil	10 keV He	Fe-10Cr CNA3 14YWT	600 900	6.82×10^{19}	~12,000	~900
Bulk	275 keV He	Fe-9Cr CNA3 14YWT	500 700	1.28×10^{20}	~8,000	~3,000

2.4 TEM characterization

Microstructure examination was performed using a 300 kV Hitachi 9000 NAR TEM, a ZEISS Libra 200HT FE MC TEM, and a 200 kV Cs-corrected JEOL JEM-ARM200F S/TEM. The thickness of the sample was evaluated from low-loss EELS spectra (Zero-loss and Plasmon-loss) using the log-ratio method. [27]. We performed thickness mapping (Figs. A.2-4) of the FIB and electropolished samples to quantify the thickness of the TEM investigated areas. The number density and volume fraction [26] of bubbles were obtained from TEM under- and over-focused images (Fig. A.5). TEM magnifications of 100 or 200 kx were used for measuring the bubble sizes. Analysis of the STEM-EELS data was performed using Gatan GMS software. The morphologies of various types of nano-particle were demonstrated by elemental maps acquired by STEM-EELS. The STEM-EELS and STEM-imaging conditions are provided in the supplemental file. The error bars in the figures considered the statistical counting errors and EELS thickness measurement errors (assumed ± 20%) using general error propagation methods.

3 Results

3.1 Bubble formation of in-situ He-implanted Fe-10Cr alloy and NFAs

We performed in-situ helium implantation on TEM samples of high purity Fe-10Cr alloy and two nanostructured alloys (14YWT and CNA3) utilizing the IVEM facility at Argonne National Laboratory. As shown in Fig 3, He bubbles were observed in all of the He-irradiated materials at 600 and 900 °C. The bubbles are visible in the matrix and also at the grain boundaries. For the Fe-10Cr model alloy, the mean matrix bubble diameter significantly increased from 2.8 nm to 14.4 nm with elevated temperature. Conversely, the matrix bubble

density decreased from 6.3×10^{22} to 2.5×10^{21} m^{-3} at 600 and 900 °C, respectively. At the same temperature range, in CNA3, the average bubble diameter increased from 3.3 to 5.7 nm, and the density slightly decreased from 2.9×10^{22} to 1.5×10^{22} m^{-3} with increasing temperature. The variation of bubble size and density with irradiation temperature was more moderate for the 14YWT alloy. The average bubble diameter slightly increased from 1.8 to 2.1 nm between 600 and 900°C. However, at both 600 and 900 °C, the bubble density of 14YWT remained almost constant around 2×10^{23} m^{-3}. In general, the average bubble size in the matrix was in the order of Fe-10Cr > CNA3 >14YWT, while the cavity density showed exactly the opposite sequencing.

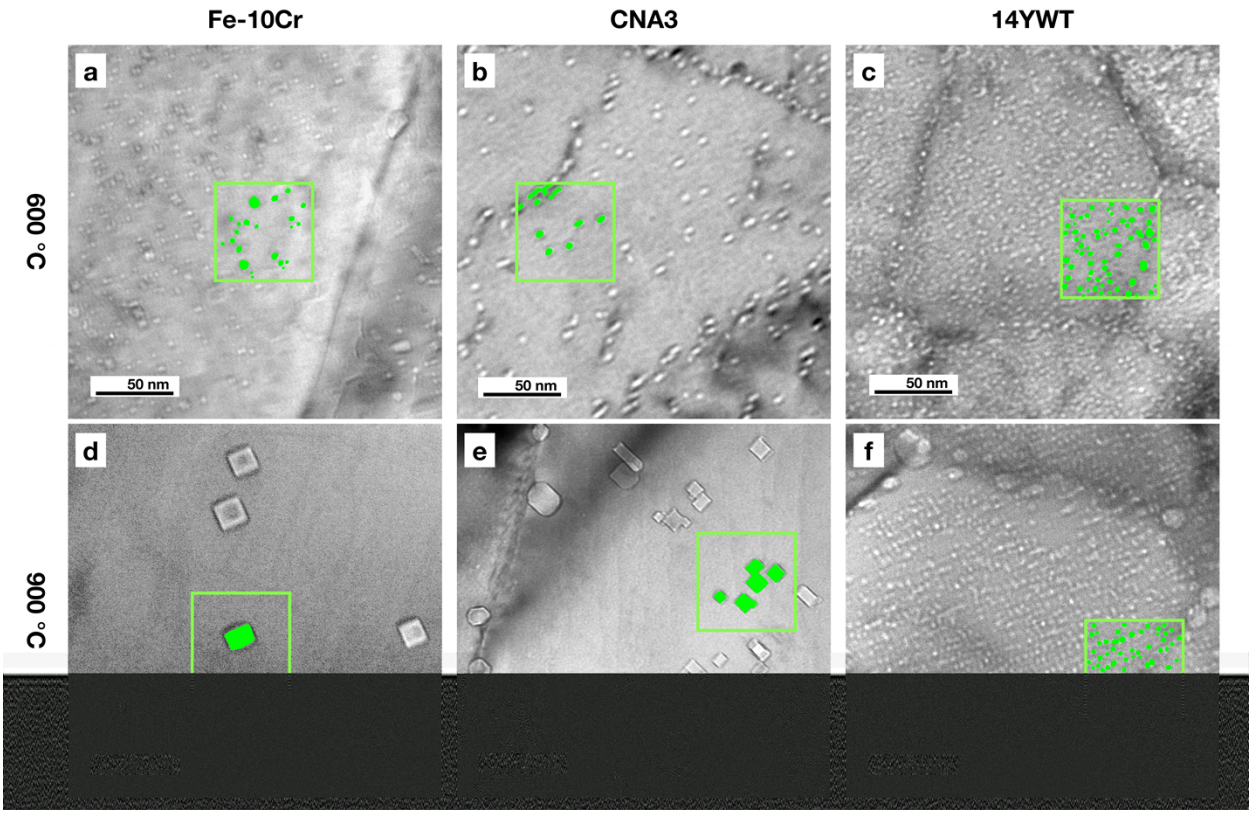

Fig. 3. Under-focused TEM images of bubbles in in-situ He implanted Fe-10Cr and NFA thin foils at 600 °C (a-c) and 900 °C (d-f).

Fig. 4 provides TEM images of the cavities in the He-implanted samples annealed at 750 and 900°C. These samples were irradiated at 600 °C (for ~15 min) and then annealed at 750°C (for ~15 min) and 900 °C (for ~15 min). The temperature was reduced to below 150°C during the interval between irradiation and annealing. Similar to the hot-implanted results, bubbles were visible in both grain matrices and grain boundaries. Also, the bubble size gradually increased from 600 to 900°C. Comparing the 900°C annealing results with the 900°C directly hot implanted experiments, the bubble size was only slightly larger in the annealed 14YWT and CNA3 samples, while the average bubble diameter of Fe-10Cr was 6 nm for the 900°C annealed case compared to 14.4 nm observed in the 900°C directly implanted sample. On the other hand, the density decreased relatively less than the directly hot implanted experiments for all of the three materials. The bubble density remained constant for the annealed 14YWT alloys. At 600°C, it is worth noting that the visible bubble density of CNA3 was lower than the Fe-10Cr alloy (Figs. 3a and 3b). However, the bubble density in CNA3 abnormally went up when annealed at 750 °C (comparing Fig. 3b to Fig. 4b). It is considered likely that a portion of small cavities (diameter below 2nm) in the CNA3 alloy, irradiated at 600 °C, may not be detected and counted by the Fresnel contrast imaging technique.

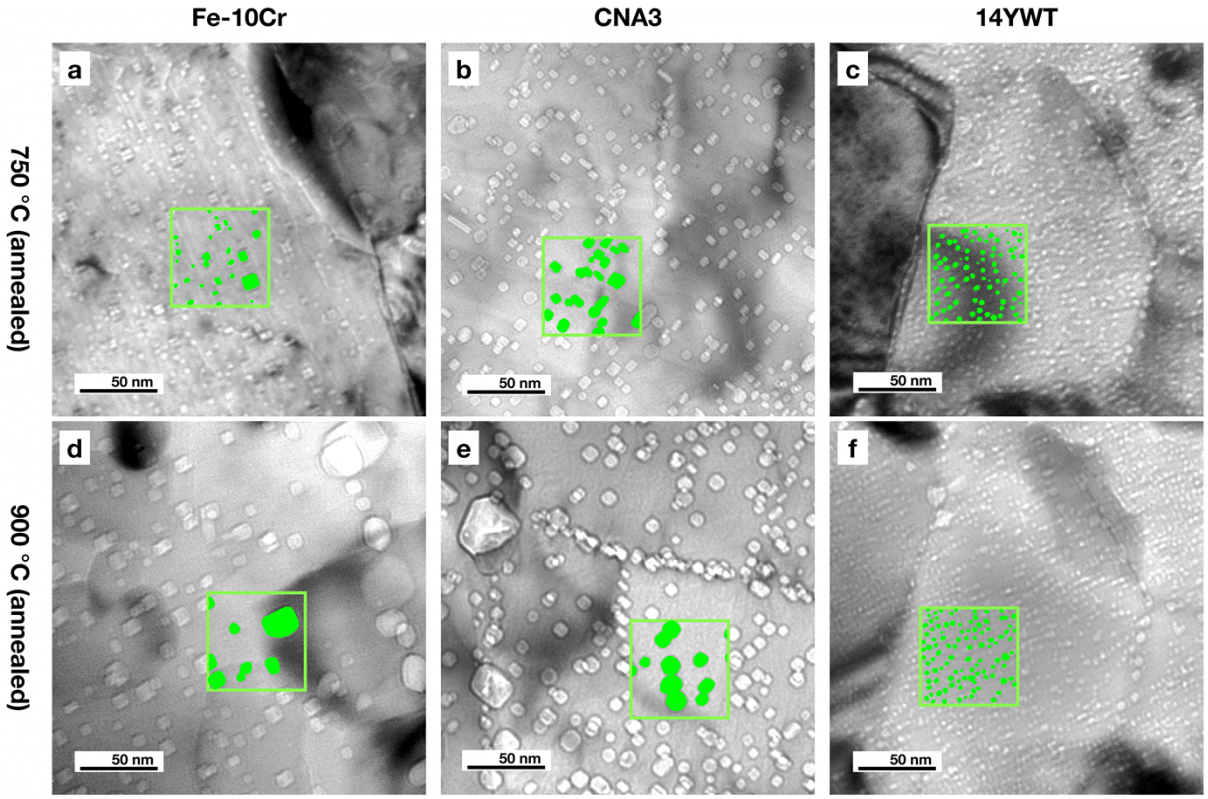

Fig. 4. Under-focused TEM images of bubbles in post-irradiation annealed Fe-10Cr and NFA thin foils at 750 °C (a-c) and 900 °C (d-f).

Fig. 5 summarizes the average size and density of the He bubbles in the Fe-Cr grain matrix. The dense-filled bars represent the directly hot-implanted experiments, and the sparse-filled bars are the 600°C implanted specimen followed by sequential annealing at 750 and 900°C. The annealed time and direct implantation both took ~15 minutes at each temperature. From 600 to 900°C, the general trend showed that bubble size increased and the density decreased in Fe-10Cr and CNA3. However, the visible bubble size and density for 14YWT remained constant within the listed error bars. The changes were most pronounced for Fe-10Cr and relatively moderate for the two alloys with nanoparticles.

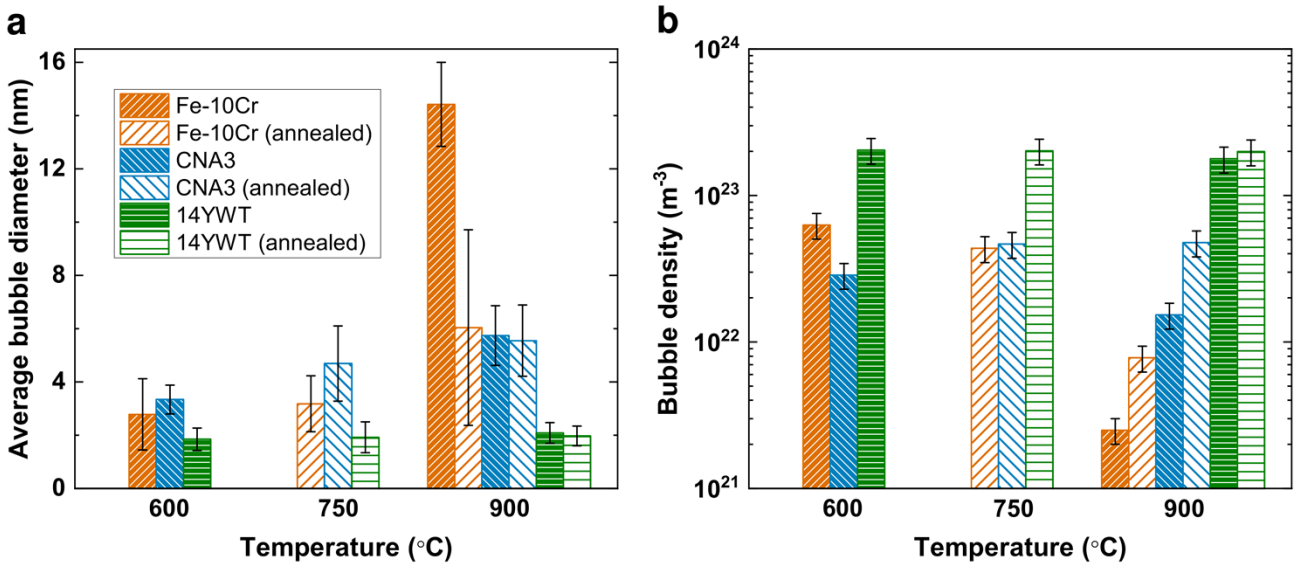

Fig. 5. Comparison of the (a) average size and (b) density of bubbles in the in-situ irradiated Fe-10Cr and NFA thin foils at 600-900 °C.

3.2 Bubble formation of ex-situ He-implanted bulk Fe-9Cr alloy and NFAs

For the study on bulk irradiated materials, 275 keV He ions were used to irradiate a Fe-9Cr alloy and the two nanostructured alloys (14YWT and CNA3) at 500 and 700°C with a fluence of 1.28×10^{20} m^{-2}. Based on the SRIM calculation, the peak radiation damage (at ~700 nm) and He concentration were roughly 0.3 dpa and 8000 appm, respectively. Figs. 6 and 7 show the cavity distribution of the three materials following He implantation at 500 and 700°C in cross-sectional TEM images. Cavities are visible in the He-implanted region for all of the six ex-situ irradiated samples. The peak damage depth at ~700 nm is indicated in red dashed lines in both Figs. 6 and 7. Most of the cavities were distributed in the range of 500-800 nm from the implanted surface. However, for the 700°C He-implanted Fe-9Cr model alloy (i.e., without the addition of nanoparticles), bubbles were agglomerated along the primitive dislocations/grain-

boundaries showing a heterogeneous distribution. This is evidence that He bubble precipitation can be more heterogeneous at high temperatures, due to higher mobility of small He-vacancy clusters compared with lower temperatures (discussed in detail elsewhere [24]).

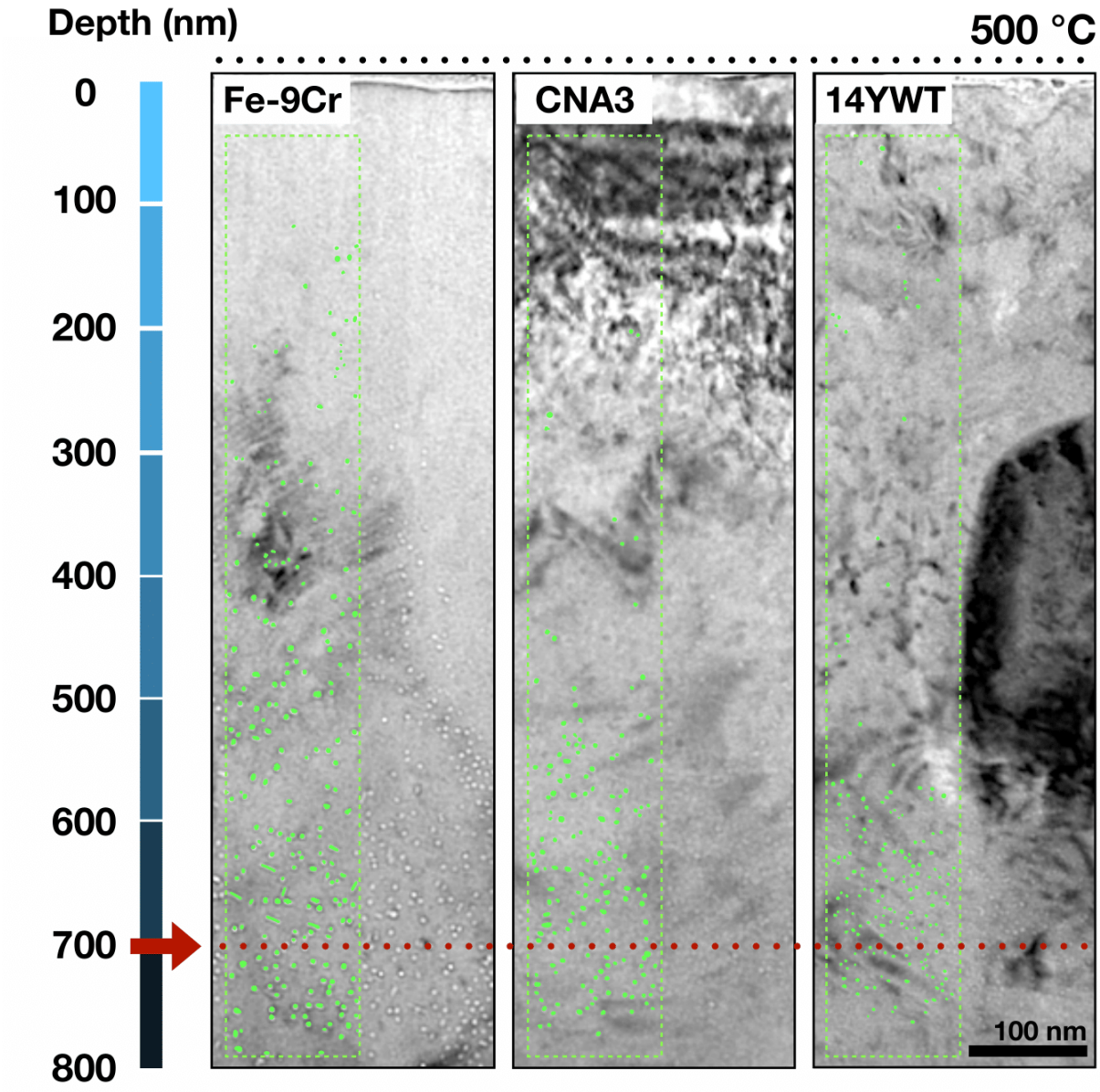

Fig. 6. Cross-sectional defocused TEM images of the bubble distribution in He-implanted bulk Fe-9Cr and NFAs at 500°C

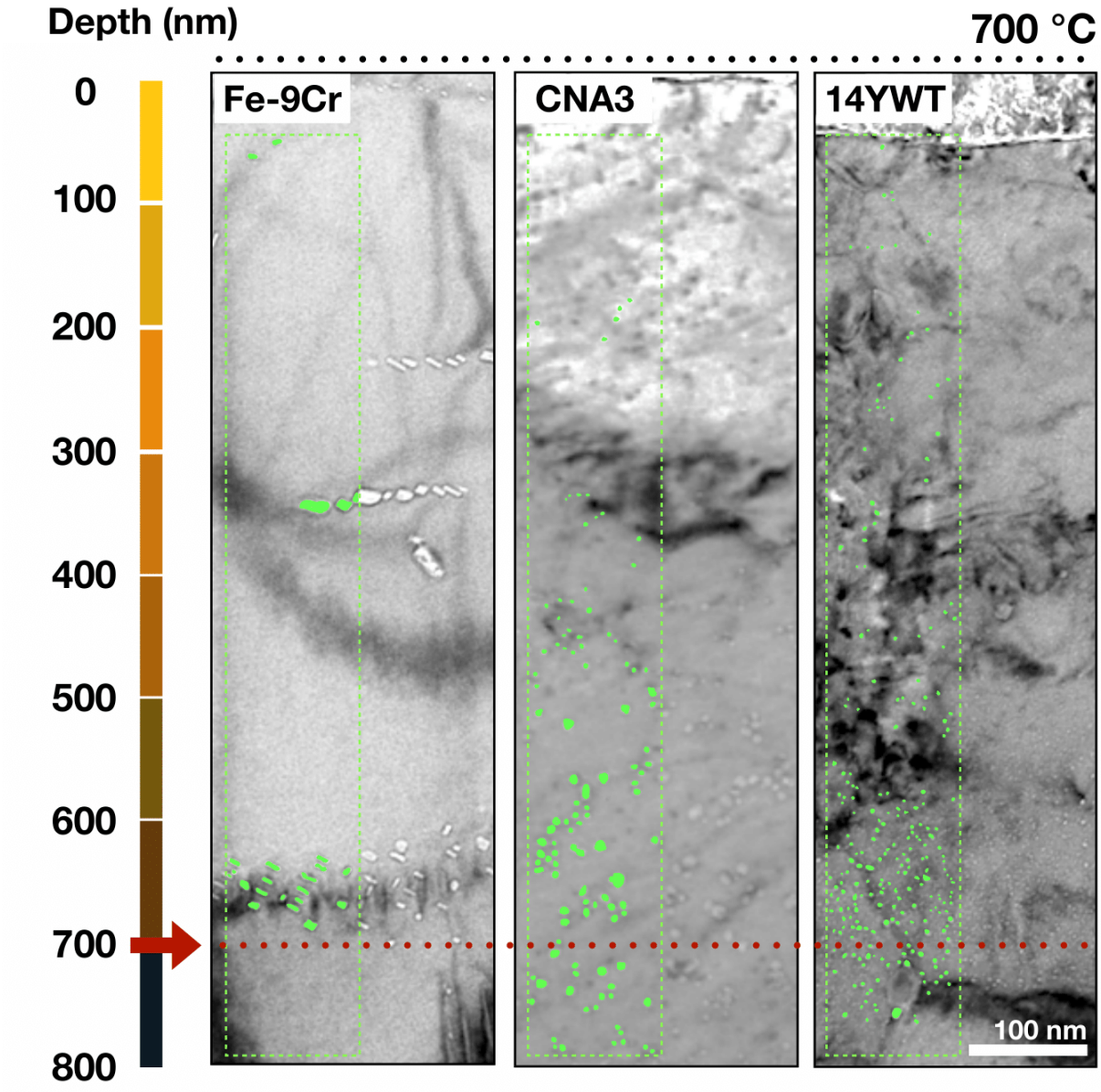

Fig. 7. Cross-sectional defocused TEM images of the bubble distribution in He-implanted bulk Fe-9Cr and NFAs at 700°C

To quantify the bubble size and density, higher magnification TEM images of all the samples were taken near the depth of 700 nm, as shown in Fig. 8. TEM examinations showed

that the size of the bubbles increased with increasing irradiation temperature, while the bubble density decreased with increasing temperature. The bubble size and density measurement results are plotted in Fig. 9. At both 500 and 700°C, Fe-9Cr (without nanoparticles) had the largest average diameter (3.7 and 8.8 nm, respectively) and the lowest density (1.0×10^{23} m^{-3} and 2.0×10^{22} m^{-3}, respectively). In accordance with the in-situ results, the bubble size of the irradiated bulk samples was also in the order of Fe-9Cr > CNA3 >14YWT, and the density had the opposite sequencing. Considering the temperature effect, the size increment and density decrement also have the same order, i.e. for a given implanted material the smallest size and largest density occurred at the lower temperature. Looking at the two materials with the lowest and highest nanostructure density, with increasing temperature (from 500 to 700 °C) the cavity sizes in Fe-9Cr and 14YWT increased by a factor of 2.35 and 1.01, respectively. Regarding the density dependence on temperature, Fe-9Cr and 14YWT decreased by a factor of 5.33 and 1.37, respectively.

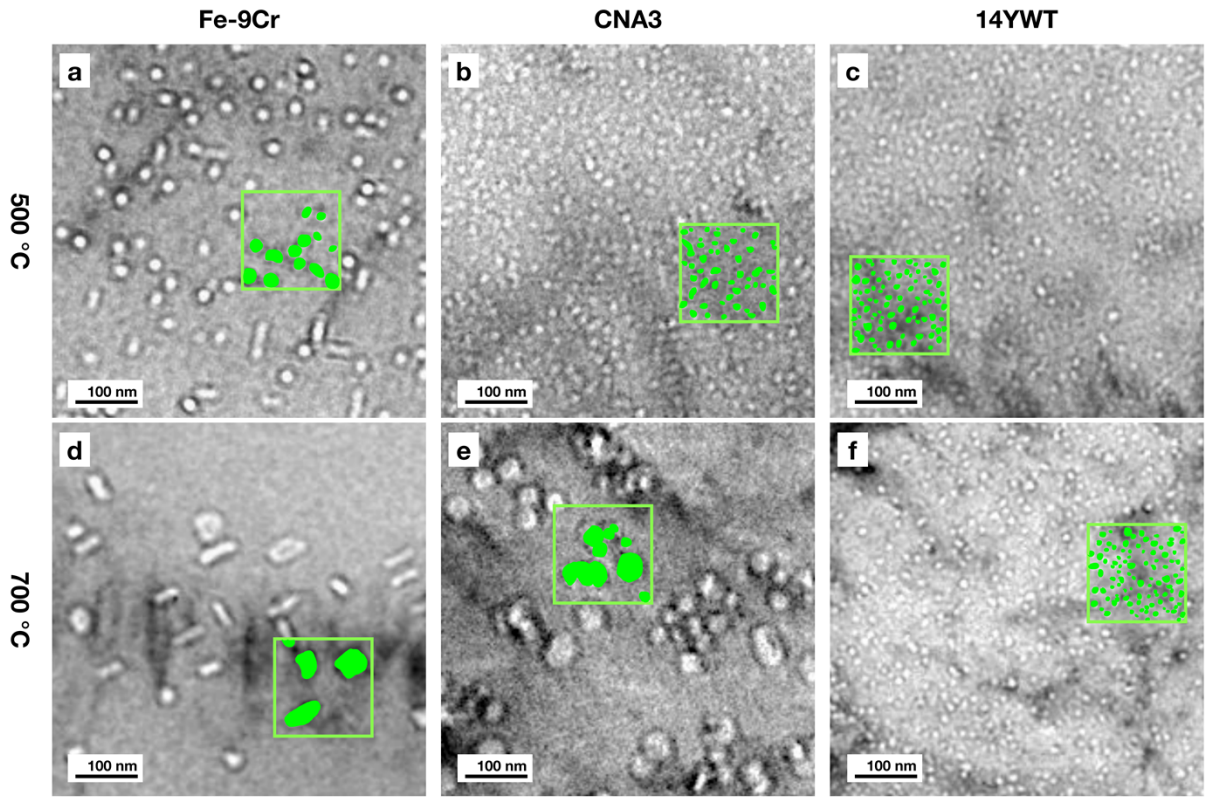

Fig. 8. Under-focused TEM images of bubbles in He implanted bulk Fe-9Cr and NFAs at 500 and 700 °C

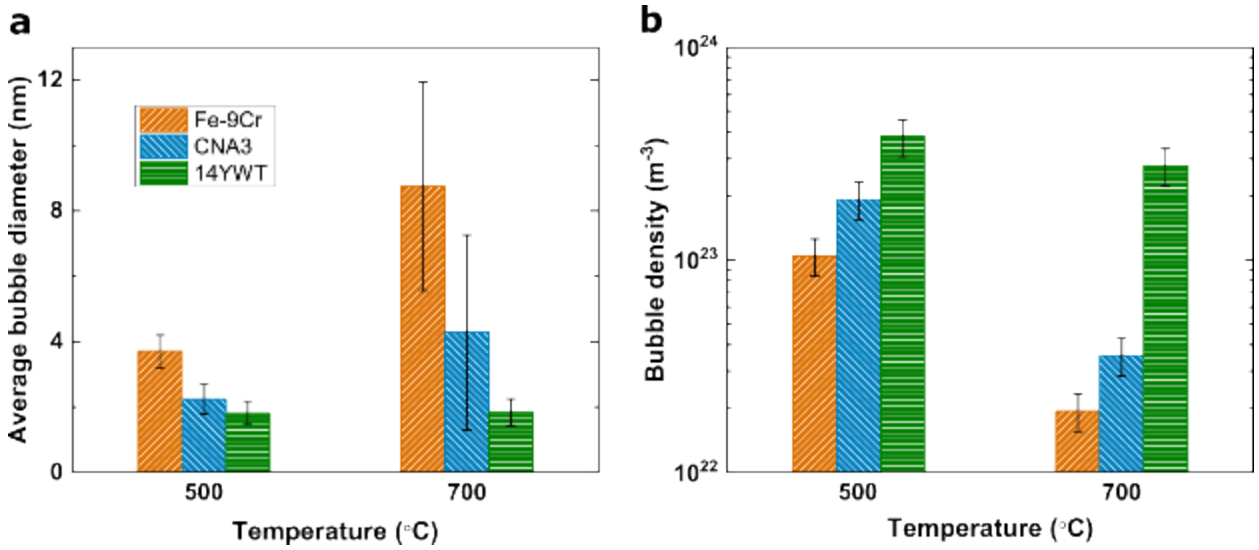

Fig. 9. Comparison of the (a) average size and (b) density of bubbles in bulk Fe-9Cr and NFAs at 500 and 700 °C.

3.3 STEM and EELS characterization on bubbles attached to nanoparticles

Previous APT and TEM results showed that the nanoparticle density of 14YWT [12] and CNA3 [9] alloys were around 10^{23}-10^{24} and 10^{21}-10^{22} m^{-3}, respectively. These nanoparticle densities are consistent with our EELS elemental mapping results (Figs. 10-13). The cavity appears dark in the STEM annular dark-field (ADF) images, which is opposite to the TEM bright-field images. As shown in our EELS results, the nanoclusters in 14YWT were mainly Y-Ti-O nanoclusters (Fig. 10), whereas coarse Ti-N particles were also observed (Fig. 11). Cr segregation was observed on the bubble surface in 14YWT, but not in CNA3. Note that the schematic diagram (in Figs. 10-13) of nano-particles and cavities are produced from projected images. The exact 3D position of the nano-particles and cavities is undetermined.

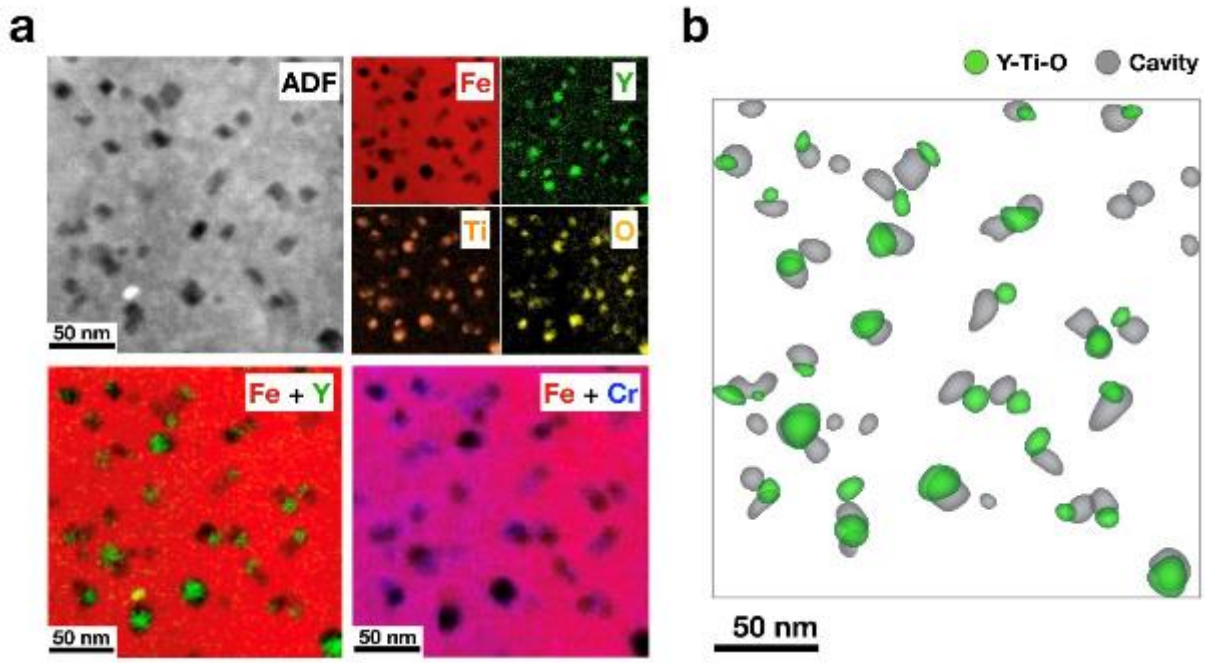

Fig. 10. (a) STEM-EELS elemental mapping of ex-situ He implanted 14YWT at 700 °C. (b) Schematic diagram of Y-Ti-O nano-particles and cavities based on Fig. 10a.

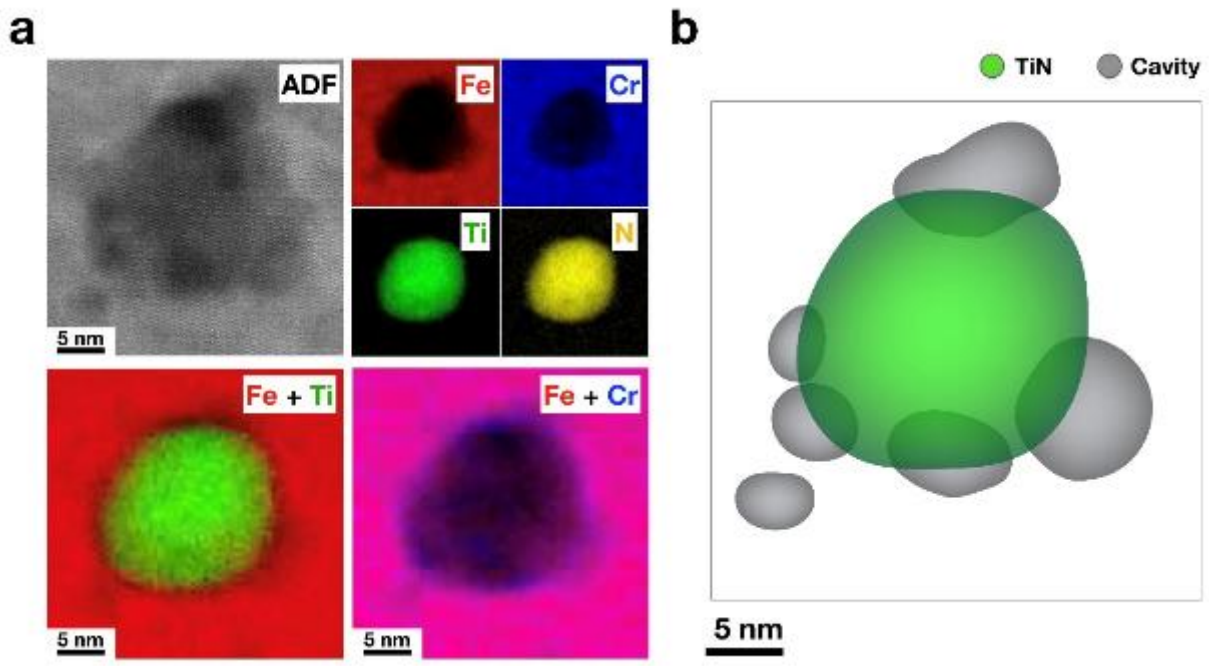

Fig. 11. (a) STEM-EELS elemental mapping of ex-situ He implanted 14YWT at 700 °C. (b) Schematic diagram of Ti-N nano-particles and cavities based on Fig. 11a.

The MX precipitates (M=Ti, W, V, Ta; X=C, N) were observed in the EELS result of CNA3 (Figs. 12 and 13). In Figs. 12 and 13, the elemental mapping of W, V, and Ta have the same site distribution as Ti. Our EELS elemental mapping results are qualitatively consistent with other atom probe tomography (APT) results of CNA3 with primarily (Ti, W, V, Ta)C particles. However, we also observed that a few of the domains were lack of MX particles. Fig 12 shows a lonesome particle overlapped with possible oxides. Other studies indicated that inclusions (oxygen- and/or nitrogen-rich) in the CNA3 materials may affect the distribution of MX particles.

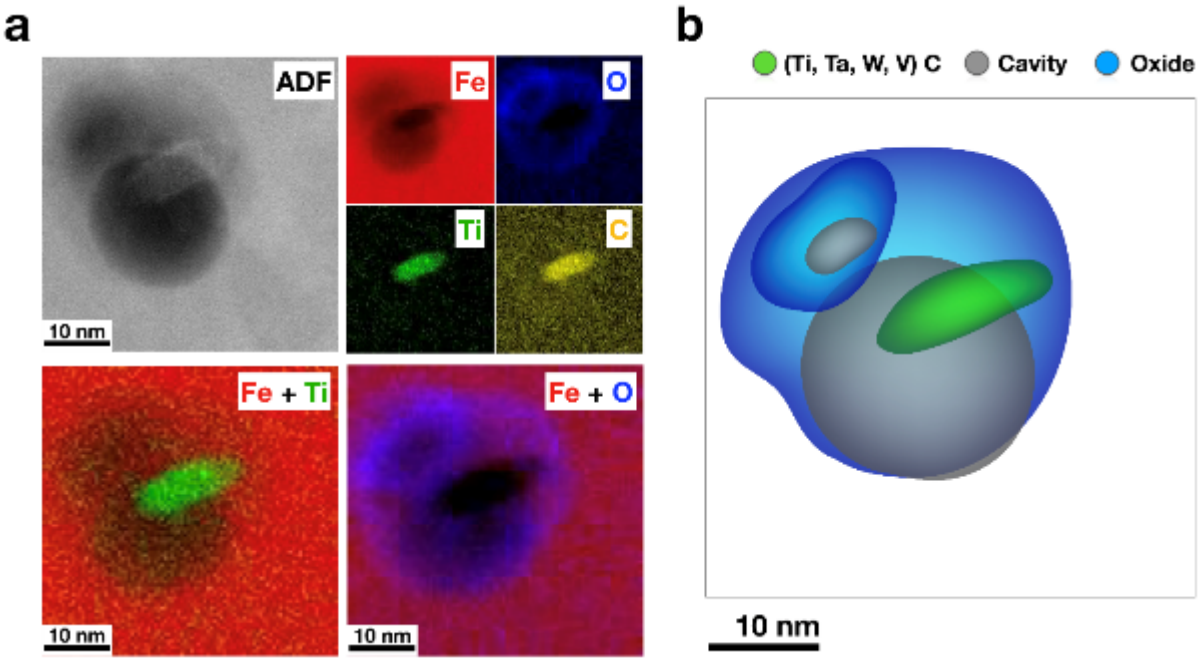

Fig. 12. (a) STEM-EELS elemental mapping of ex-situ He implanted CNA3 at 700 °C (W, V, Ta have the same site distribution as Ti). (b) Schematic diagram of a (Ti, W, V, Ta)C nanoparticle, oxides, and cavities based on Fig. 12a.

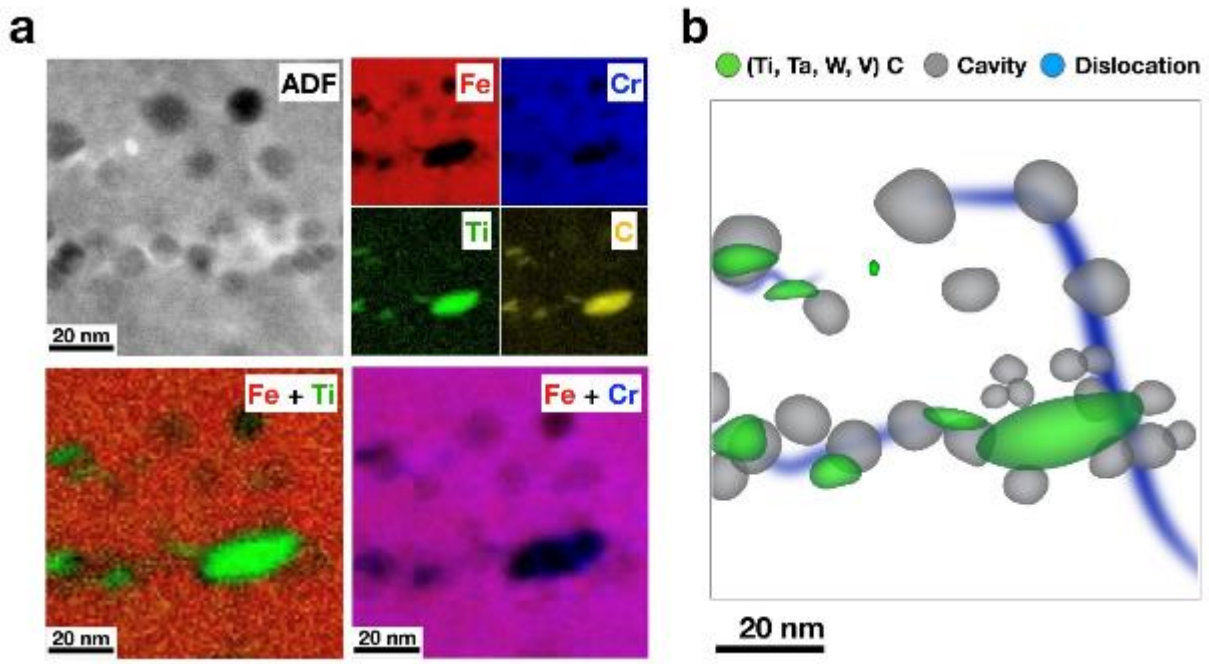

Fig. 13. (a) STEM-EELS elemental mapping of ex-situ He implanted CNA3 at 700 °C (W, V, Ta have the same site distribution as Ti). (b) Schematic diagram of (Ti, W, V, Ta)C nano-particles, dislocations, and cavities based on Fig. 13a.

The four types of investigated nanoparticles all showed good capability for trapping He bubbles. Among our EELS results, the Y-Ti-O nanoclusters in 14YWT have the most uniform distribution and exhibited a one-to-one relationship for bubble attachment to the Y-Ti-O nanoclusters. The (Ti, W, V, Ta)C dispersoids in CNA3 attached ~3-10 small He bubbles to a single particle. In the CNA3 sample irradiated at 700°C, some bubbles were observed to be trapped not by nanoparticles but by network dislocations (Fig. 13). The same phenomenon is clearly revealed by STEM images in the same CNA3 irradiated sample (Fig. 14), where bubbles appeared at the nodes of dislocation networks.

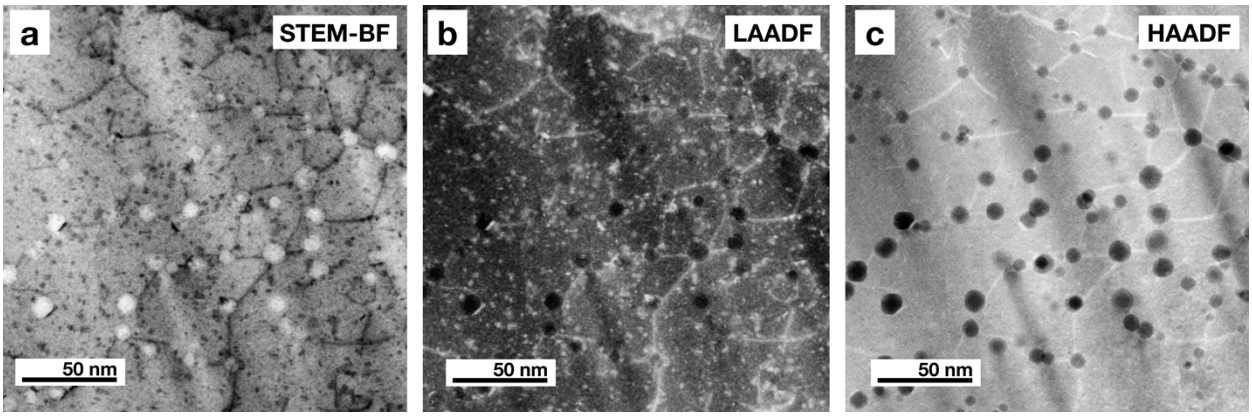

Fig. 14. STEM images of cavities in ex-situ He implanted CNA3 alloy at 700 °C, showing preferential location of cavities on intersecting dislocations: (a) STEM-BF, (b) STEM-LAADF, and (c) STEM-HAADF

The difference between the low-angle annular dark-field (LAADF) and the high-angle annular dark-field (HAADF) images is the collection angle of the detector [28-30]. LAADF images would still show diffraction contrast or difference of specimen thickness dependence due to the partial collection of Rutherford scattering (elastic) signal which dominates at lower angles. HAADF images collect thermal diffuse scattering (quasi-elastically) signals and are more sensitive to the atomic number.

4 Discussion

4.1 Overall bubble behavior

In Fig. 15, for both ex-situ and in-situ experiments, with increasing temperature from 500 to 900°C, the general trend showed that bubble size increased and the density decreased for the

three alloys, as expected based on simple cavity coarsening expectations. The 14YWT alloy appears to sequester the helium into smaller bubbles more effectively, and has the highest bubble density among the three investigated alloys at all temperatures. The CNA3 alloy exhibited good He trapping at 500 and 600°C but relatively inefficient trapping at 700 and 900°C, based on the decrease in measured cavity density and the observation of cavities preferentially attached to dislocations rather than exclusively being associated with MX particles (Fig. 14). This may indicate that MX particles in CNA3 may not be stable or have a lower He binding energy (lower He trapping ability) at high temperatures above 700°C. In addition, above 700°C, the irradiation temperature approaches the austenite transformation temperature, generally only evident above 848 °C for 8-10 at% Cr, in iron-chromium binary system [31]. Therefore, phase transformation has a chance to occur in the matrix and affect the formation of bubbles for the high temperature anneals (especially at 900°C). Generally, the cavity swelling resistance of body-centered cubic metals (e.g. ferritic/martensitic steels) is superior to that of face-centered cubic metals (e.g. austenitic steels) [5, 32].

Dauben et al. [23] and Yan et al. [24] reported two different activation energies at low-temperature and high-temperature regimes for helium in Fe-Cr alloys. The activation energies were evaluated from the line slope of the Arrhenius plot of bubble size (or bubble density) vs. inverse temperature. The activation energies exhibit a weak dependence on temperature below ~600°C and a stronger temperature dependence above ~600°C. Yan et al. suggested that the activation energy difference is related with different point defects evolution stage at different temperatures [24] Dauben et al. inferred that the activation energy for bubble size (E_R^{act}) is one-quarter or one-sixths of the helium migration energy at the low-temperature regime [23]. For the high-temperature regime (> 600°C), the increment of activation energy could attribute to helium

desorption or migration of helium bubbles [33]. In Fig. 15, Arrhenius plots were illustrated for the He implanted materials to compare the effective activation energies and their temperature dependence. The 600 and 800°C data for Fe-9Cr in Fig. 15 are reproduced from the study by Yan et al [24], where a same Fe-9Cr material and irradiation facility were used. The estimated activation energies for bubble size (E_R^{act}) and density (E_N^{act}) are summarized in Table 2. The activation energy (obtained from the linear regression slope) of Fe-9/10Cr are in consistent with previous studies [23, 24] showing a surge/drop at around 600°C (Fig. 15). Overall, the E_R^{act} of model Fe-Cr alloys is in the range of 0.11-0.17 and 0.48-0.82 eV for the low- and high-temperature regime, respectively. The E_N^{act} of Fe-Cr alloys is 0.17-0.21 and 0.86-1.95 eV for low and high temperatures, respectively. However, the two NFAs did not show distinct activation energies in the two temperature regimes. The activation energies of CNA3 are in-between the low- and high-temperature activation energies of Fe-9/10Cr, while the activation energies of 14YWT are even lower than the low-temperature activation energies of Fe-9/10Cr. This indicates that nanoparticles in NFAs can impede the helium motion. It is suggested that, at high irradiation temperatures (> 600°C), a sufficient He binding energy of bubble attached to nanoparticles could suppress the helium desorption or migration of helium bubbles in the Fe-Cr matrix.

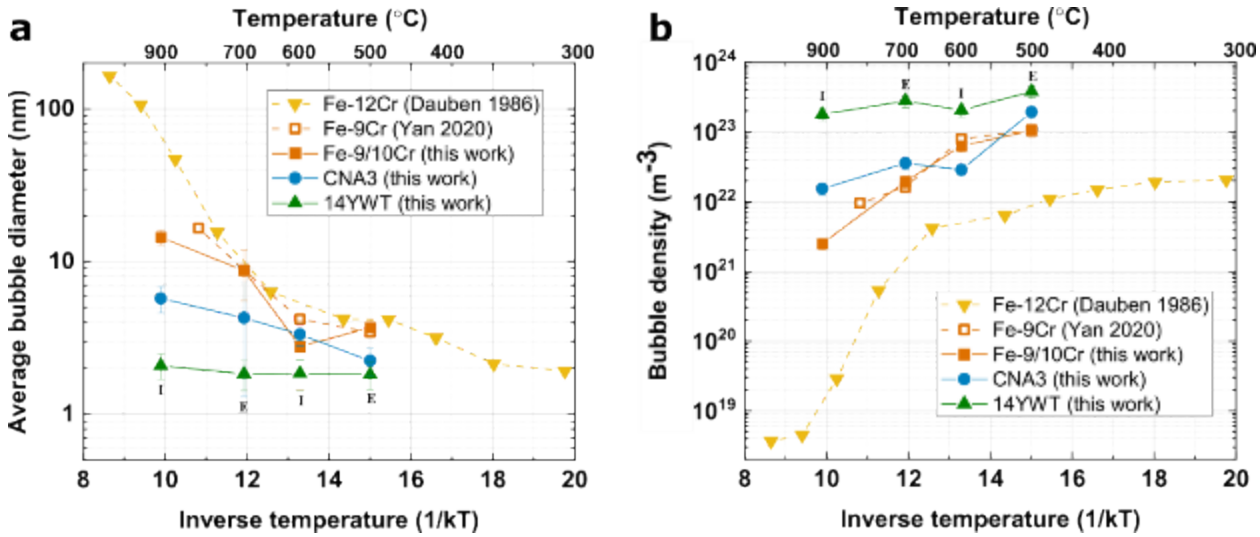

Fig. 15. Arrhenius plot of (a) bubble size and (b) density as a function of inverse absolute temperature. The "I" and "E" labels in the figures stand for in-situ irradiation and ex-situ irradiation, respectively. (ref. [23, 24])

Table 2. Effective activation energy for bubble size (E_R^{act}) and density (E_N^{act}) obtained from the Arrhenius plot in Fig. 15.

Activation energy (eV)	Fe-12Cr [23]	Fe-9Cr [24]	Fe-9/10Cr	CNA3	14YWT
E_R^{act}	0.17±0.06* & 0.82±0.08**	0.12* & 0.64**	0.11±0.02* & 0.48±0.01**	0.18±0.02	0.02±0.01
E_N^{act}	0.21±0.05* & 1.95±0.21**	0.17* & 0.99*	0.17±0.05* & 0.86±0.20**	0.45±0.16	0.12±0.07

*Experiments at temperatures below 600 °C
**Experiments at temperatures above 600°C

Cavity swelling (estimated by calculating the total volume of each spherical bubble with respect to the volume of the analyzed zone) increased steadily with increasing irradiation and/or annealing temperature (Fig. 16). At the same temperatures, the 14YWT alloy showed the lowest

total volume swelling, while Fe-9/10Cr had the largest swelling value. Further, the Fe-9Cr ex-situ specimen exhibited higher swelling at all temperatures compared to the in-situ Fe-10Cr specimen. At comparable temperatures, the bubble density is lower in the in-situ studies. This could partially due to the low-swelling surface effect of in-situ irradiated thin foils or the difference in grain size, impurity, and primitive dislocation density between the two binary alloys. Also, the swelling variation with increasing temperature was much more moderate for the 14YWT alloy, which had the highest nanocluster density. With the same amount of implanted He content, both the ex-situ and in-situ experiments infer that distributing He to a higher density but smaller size of bubbles could reduce the total swelling value. This is evidence that the dispersoids in both of the nanostructured alloys (particularly 14YWT) were rather effective in trapping He-vacancy complexes at their dispersoids. In addition, once these bubbles formed on nanoparticles, they could act as sinks for He as well as point defects (vacancies or interstitials). Further study on the He content in the bubbles and the He binding energy of bubbles attached to nanoclusters, dislocations, or grain boundaries would be useful to understand the detailed mechanism of the formation of bubbles in nanostructured alloys.

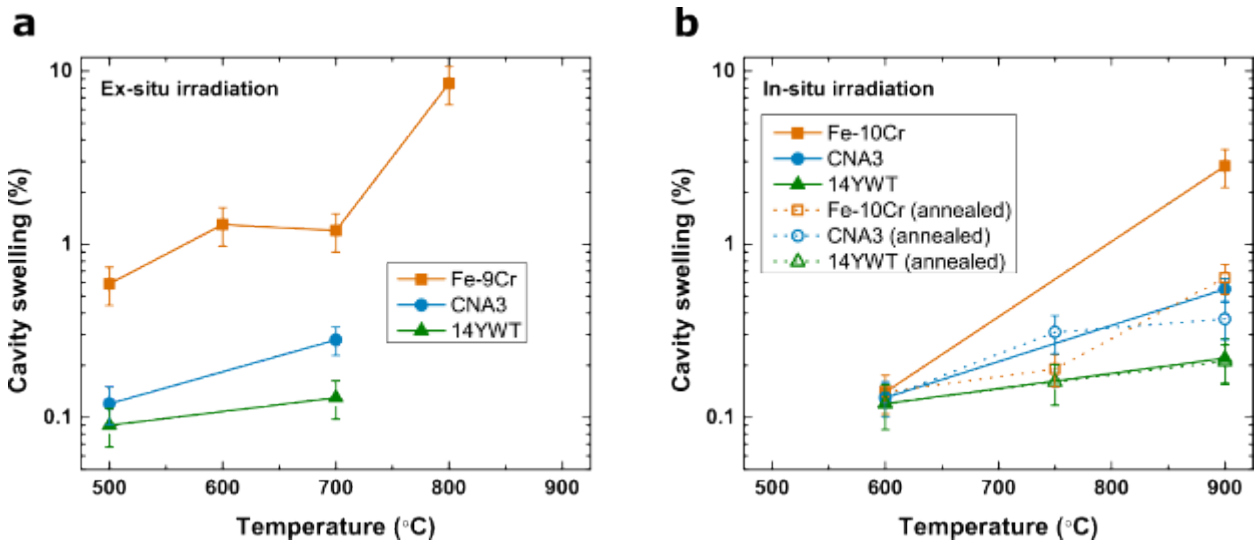

Fig. 16. Cavity swelling of the (a) ex-situ (bulk) and (b) in-situ (thin foil) irradiated Fe-9/10Cr alloy and NFAs at 500-900 °C. The Fe-9Cr swelling values in Fig. 16a are reproduced from ref.[24]

For the ex-situ irradiated bulk materials, apart from examining the bubbles near the peak He concentration depth (~700 nm), it is also worth understanding the overall bubble distribution from the sample surface to depth >700 nm. Fig.17 illustrates the depth distribution of the number of bubbles in the irradiated bulk materials (see Figs. 6 and 7 for the cross-sectional defocused TEM images). As shown in Fig. 17, the bubble distribution is concentrated near the peak He concentration depth (~700 nm), which is in agreement with the SRIM estimation (Fig. 1b). At 700°C (Fig. 17b), the cavity number fraction in 14YWT, CNA3, and Fe-9Cr model alloy at the 500-800 nm depth interval were 76%, 70%, and 38%, respectively. This indicates that the addition of a higher density of nanoparticles could better confine the diffusion of He. However, a small amount (cavity number fraction < 3%) of He bubbles in 14YWT were observed near the sample surface (at depth < 100 nm), but not in CNA3. This may due to the much smaller mean

grain size (~0.2 μm) of the 14YWT material compared to the prior-austenite grain size of CNA3 (10-60 μm). The longer total length of grain boundaries may enhance the diffusion of He via a pipe diffusion along grain boundaries, as discussed in the next section [34].

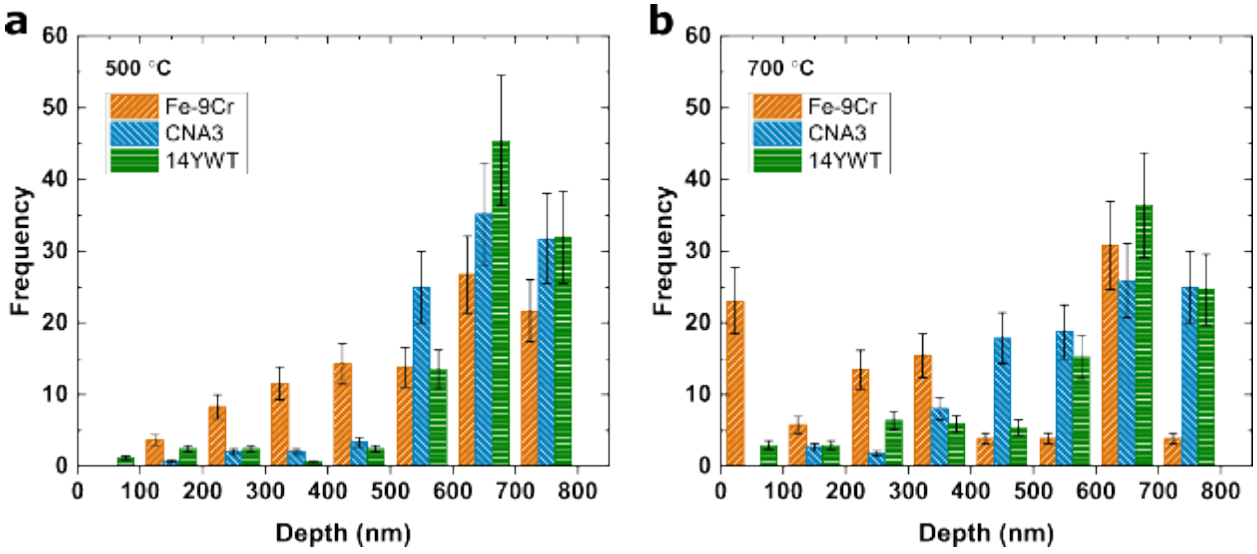

Fig. 17. Depth variation of the number of bubbles in the ex-situ irradiated bulk samples at (a) 500 and (b) 700 °C.

4.2 Bubbles in grain boundary

In addition to the evolution of bubbles in the matrix, the bubbles at the grain boundaries have also been examined. Statistical information on the bubbles at grain boundaries is summarized in Fig. 18. In the three materials, the average bubble size at grain boundaries increased with increasing irradiation temperature and with higher temperature annealing process. However, the temperature dependence of the cavity density at grain boundaries was monotonic. Also, the distribution in sizes was inhomogeneous with large standard deviations. Helium bubble

nucleation along grain boundaries is likely to be aided by the enhanced diffusion of He along grain boundaries by a pipe diffusion mechanism, which occurs with a lower activation energy [34]. At sufficiently high irradiation temperatures, vacancies became mobile and may be trapped by the grain boundaries resulting in a net growth of the bubbles [15, 35]. As shown in the in-situ post-irradiation annealed TEM images (Figs. 4d-f), because bubbles can diffuse more readily along grain boundaries due to the increased free volume, the growth of bubbles may be further facilitated by a migration and coalescence mechanism.

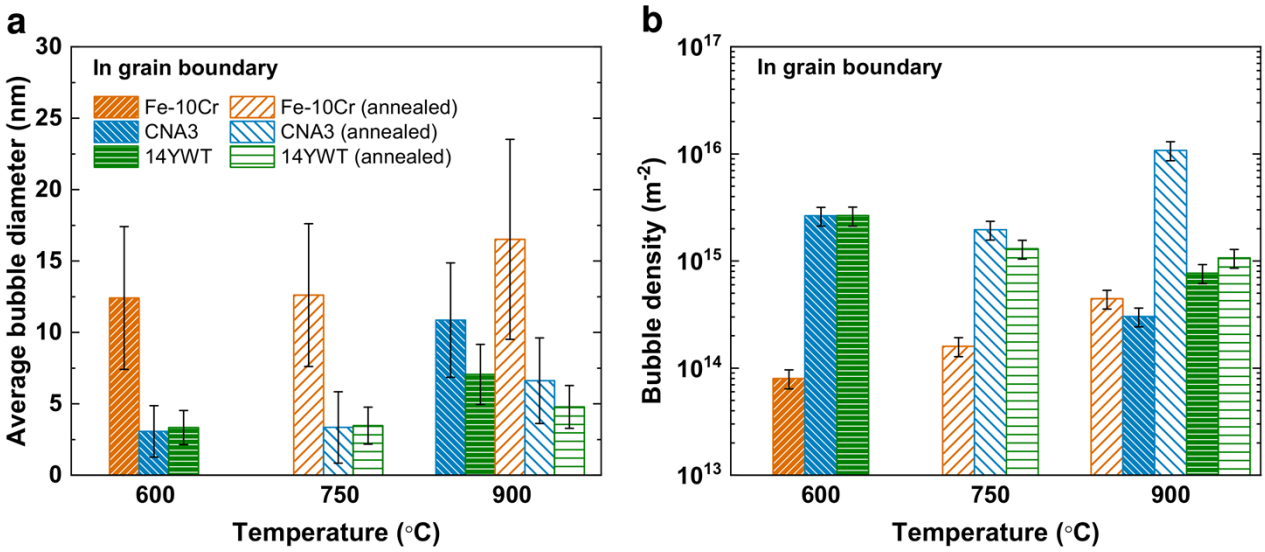

Fig. 18. Comparison of the (a) average size and (b) density of cavities at grain boundary in the in-situ irradiated Fe-10Cr and NFA thin foils at 600-900 °C.

As for the comparison between He bubbles at grain boundaries in materials with and without nanoclusters, Fig.18 shows that the grain boundary average bubble diameter in Fe-10Cr at 600 °C is 2-3 times larger than in the two nanostructured alloys. Besides, at 900 °C, grain boundary cracking was severe in Fe-10Cr (Fig. 19a). Therefore, the grain boundary bubble size and density of the Fe-10Cr sample could not be measured at this irradiation temperature. Fig. 19b shows possible traces of large faceted cavities with a side length up to ~1 μm, near and

along a grain boundary. As discussed earlier that the austenite (gamma phase) transformation temperature is about 848 °C for 8-10 at% Cr, and gamma phase Fe with FCC crystal structure has less resistance to cavity swelling. There is a possible influence of alpha-gamma phase transition-induced stresses in addition to standard thermal annealing bubble coarsening effects. This significant difference between model and nanostructured alloys in the formation of cavities/bubbles at grain boundaries demonstrates the effectiveness of nanoparticles as preferential sites for He bubble nucleation in the matrix, thereby suppressing the amount of He-vacancy clusters that diffuse to grain boundaries. This also emphasizes the ability of nanoparticles to reduce the nucleation of large He bubbles along grain boundaries that would result in the degradation of material properties (e.g. high-temperature grain boundary embrittlement).

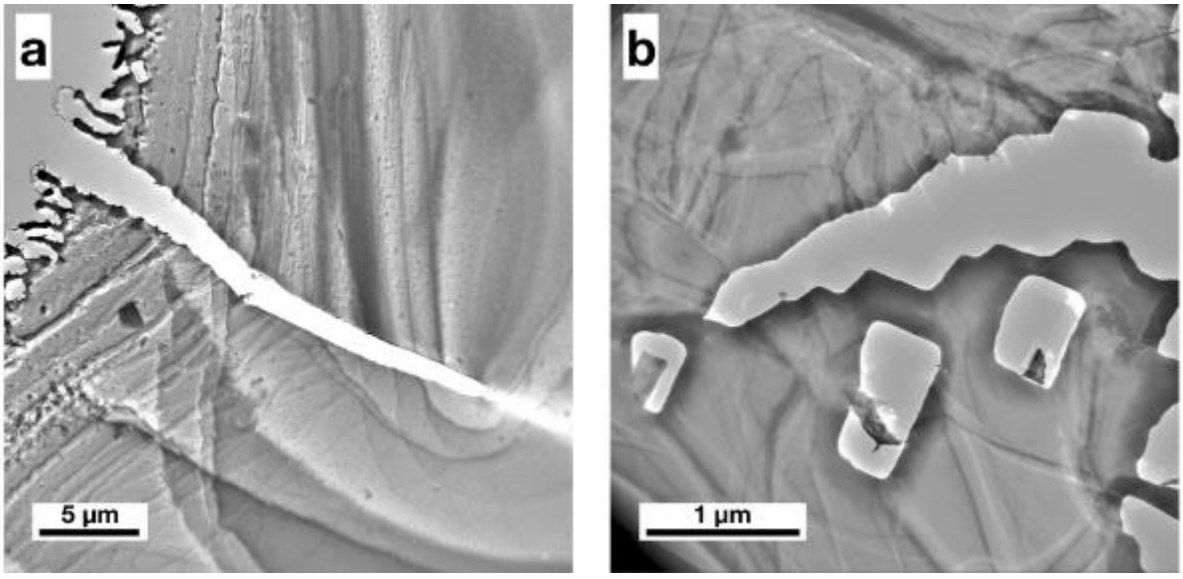

Fig. 19 TEM images of (a) grain boundary cracking and (b) possible traces of large faceted cavities/bubbles in the in-situ irradiated Fe-10Cr thin foil at 900 °C.

4.3 Relation of bubbles to nanoparticles

In Figs. 10-13, the EELS results show that the bubble number densities are comparable to the nanoparticle densities for the CNA3 and 14YWT alloys and that the He bubbles are preferentially associated with nanoparticles, suggesting that the nanoparticles are rather effective at trapping He-vacancy complexes at the particle-matrix interface. In order to further discuss the relation of bubbles to nanoparticles, the nanoparticle density as a function of cavity/bubble density in various irradiated NFAs are compiled in Fig. 20, at irradiation temperatures below and above 600°C. Note that the irradiation conditions of each data point were different: Lu et al. (460 °C, ~0.5 appm He/dpa) [36]; Parish et al. (650 °C, ~15 appm He/dpa) [16]; Brimbal et al. (460 °C, ~17 appm He/dpa) [37]; Yamamoto et al. in 2007 (500 °C, ~42 appm He/dpa) [38]; Yamamoto et al. in 2014 (650 °C, ~47 appm He/dpa) [17]; Edmondson et al. (400 °C, ~12,000 appm He/dpa) [14]; ex-situ study of this work (500 and 700 °C, ~2,700 appm He/dpa); in-situ study of this work (600 and 900 °C, ~4,000 appm He/dpa).

As shown in Fig.19, the cavity density increased with increasing nanoparticle density. Compared to the cavity density in Fe-9/10Cr (without nanoclusters) as a reference point, at irradiation temperatures below 600°C, the cavity density in several NFAs with nanoparticle density below ~10^{22} m^{-3} did not show a significant difference compared to Fe-9/10Cr model alloys. However, above 600°C, where the number of cavities in Fe-9/10Cr would dramatically decline (Fig 15b), the cavity density in NFAs remains high. Overall, the data points exhibited a 1:1 correspondence between cavity density (N_c) and particle density (N_{ppt}) within one order of magnitude deviation. The cavity density of NFAs with high particle density ~10^{24} m^{-3} showed a slight deviation of $N_c < N_{ppt}$, while the NFAs with particle density ~10^{22} m^{-3} had $N_c > N_{ppt}$. This could be related to the average nanoparticle size difference between CNA3 (~8 nm) and

14YWT (~ 4nm). As shown in or EELS elemental mapping results (Fig. 13), a single nanoparticle in CNA3 could attach 3-10 small He bubbles, and a single particle in 14YWT attaches roughly one helium bubble (Fig. 10). In other words, the nanoparticle size or surface area could also affect the N_c/N_{ppt} ratio.

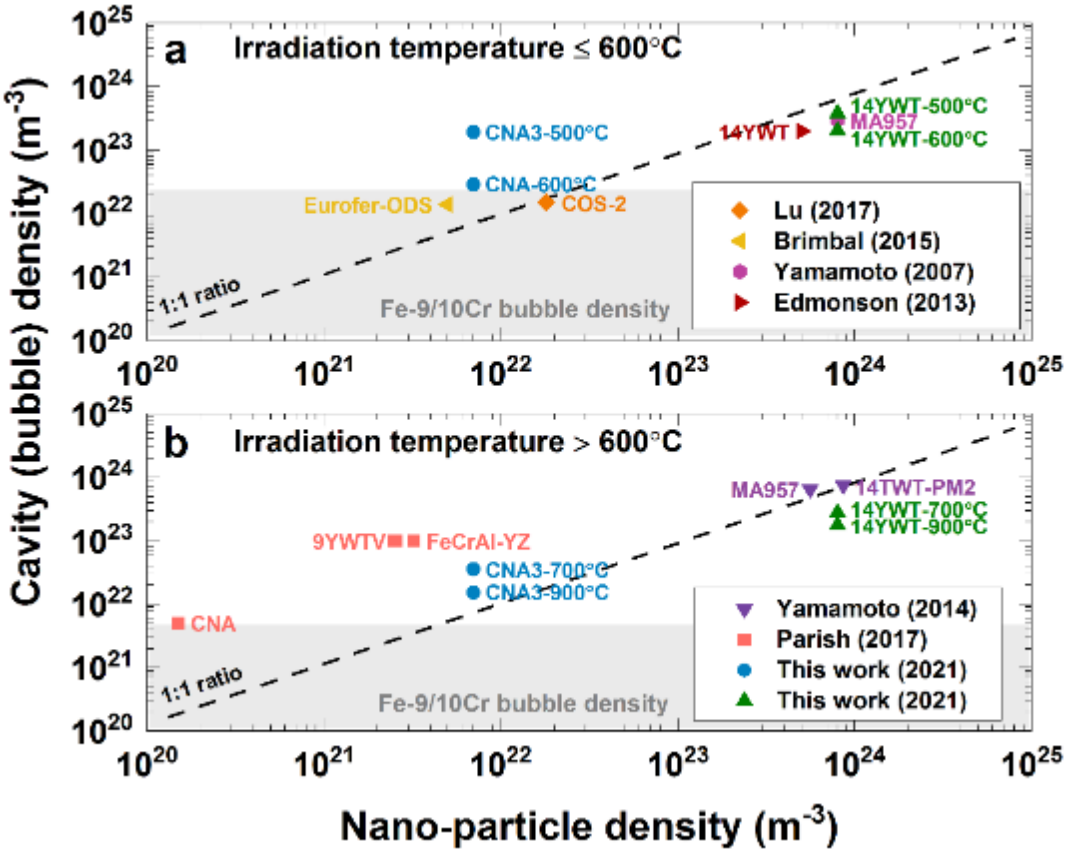

Fig. 20. Variation of bubble density as a function of nanoparticle density. (a) Irradiation temperature < 600°C, (b) Irradiation temperature > 600°C. Ref. [14, 16, 17, 36-38].

With a simplified estimation, the mean inter-particle distance ($\bar{r}$) could be calculated by:

$$\bar{r} = \frac{1}{\rho^{1/3}} \quad (1)$$

Where ρ is the nanoparticle density. Substituting the nanoparticle density of CNA3 (~10^{22} m^{-3}) and 14YWT (~10^{24} m^{-3}) into the equation finds the average interparticle distance of 46 and 10 nm, respectively. On the other hand, the implanted He can escape to a free surface (e.g. dislocations, grain boundaries, sample surface, etc.) if the mean free path (L) for He diffusion between the bubbles is larger than the distance to a free surface. The mean free path can be estimated by [23]:

$$L = \frac{1}{2}(\pi N R)^{-0.5} \quad (2)$$

Where N is the bubble density and R is the bubble radius. Take the bubble density and size in Fe-9Cr irradiated at 700°C for example, the equation gives a diffusion length of ~30 nm, which is on the same order of the average interparticle distance of nanoparticles in CNA3 (~46 nm). However, this interparticle distance is smaller than the diffusion length of ~30 nm. This could partially explain the observation of bubbles trapped by dislocations in CNA3 (Fig. 14). As for 14YWT, the mean free path is three times larger than the interparticle distance, which indicates that the He-vacancy complexes have sufficient mobility to easily diffuse the distance to a nanoparticle.

Although Fig. 20 infers that the nanoparticle density could be positively correlated with cavity density, other factors such as different types of sink strength (e.g. dislocation, grain boundary, alpha prime precipitates), the He trapping ability of the nanocluster, He per dpa ratio, the Cr effects, and temperature could all affect the formation of cavities. Based on the standard rate theory [39], approximations of the defect sink strengths for different microstructural features of the as-received materials were evaluated (see appendix for details). Our calculation results (Table A.2) showed that the total initial sink strength (unirradiated material) is dominated by the

dispersoids when the particle density is above ~10^{21} m^{-3}. The sink strength of a grain size above ~0.1 μm and dislocation density below ~1×10^{14} m^{-2} would be on an order of magnitude less than the nanoparticle sink strength (when their density is above ~10^{21} m^{-3}). Fig 21 shows the bubble size, bubble density, and swelling in the He implanted materials as a function of sink strength. The estimated total initial sink strengths of as-received Fe-10Cr, Fe-9Cr, CNA3, and 14YWT material were 1×10^{12}, 1×10^{14}, 2×10^{15}, and 3×10^{16} m^{-2}, respectively. The bubble size decreased (Fig. 21a) and the bubble density (Fig. 21b) increased with increasing sink strength. For the cavity swelling, Fig. 21c suggests that a significant decrease in cavity swelling can be achieved if the sink strength is above ~10^{15} m^{-2}, which corresponds to a nanoparticle density above ~10^{21} m^{-3}.

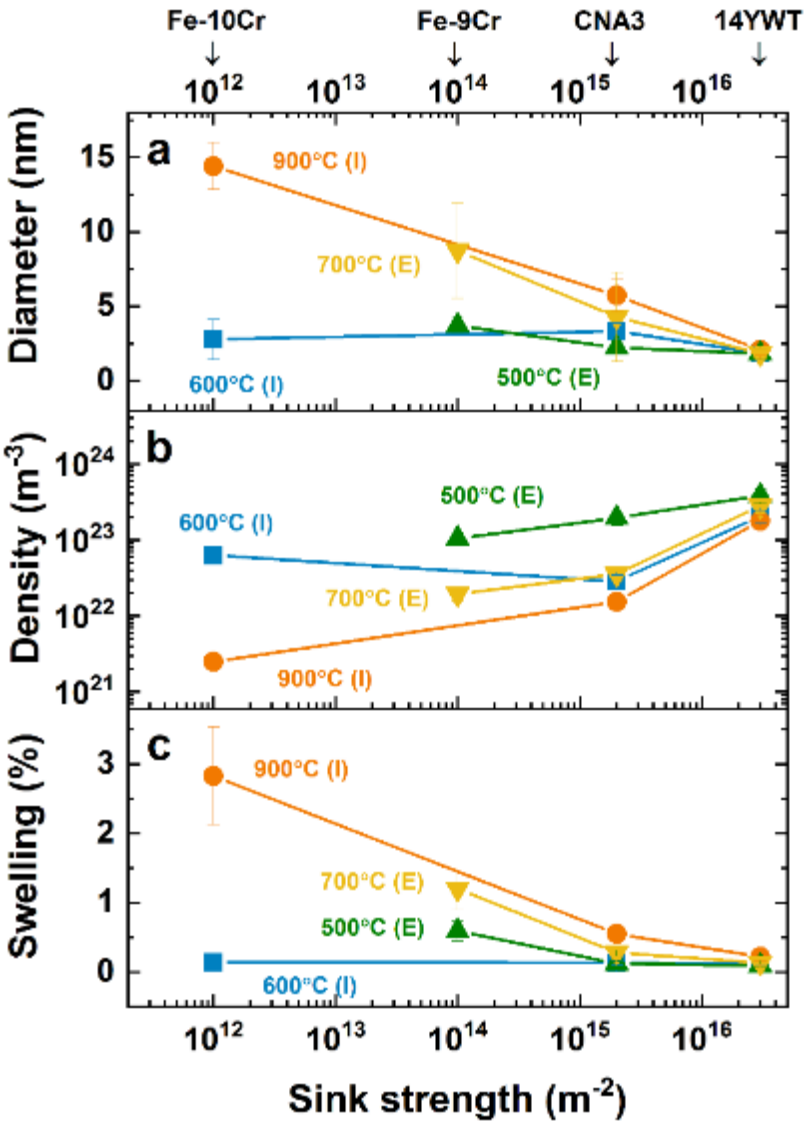

Fig. 21. Variation of (a) bubble size, (b) bubble density, and (c) swelling as a function of sink strength.

STEM-HAADF characterization was performed to identify the nanoparticle structure and the attached bubbles in the ex-situ He-implanted CNA3 and 14YWT nanostructured alloys at 700°C (Fig. 22). The HAADF scattering signal from a single column of atoms is strongly dependent on the atomic number and the number of atoms in a single atom column [28-30].

Hence, the bubbles exhibit black contrast in HAADF images due to the absence of atoms. In Fig. 22, a series of high-resolution HAADF images were taken at the junction of the bubble (B) and nanoparticle (P) (Figs. 22a-c), or junction of bubble and grain boundary (Fig. 22d). For the fine Y-Ti-O and (Ti, Ta, W, V)C clusters with diameter <10nm (Figs. 22a and 22b), the atomic structure under TEM as well as their fast Fourier transform (FFT) images taken at the B and P regions remains the same as the matrix ferritic structure. The cavity and nanoparticle with a diameter of less than ~10 nm are embedded in the matrix structure. Considering a sample thickness of ~80 nm, at least seven-eighths of the atoms in an atomic column would be the surrounding Fe or Cr matrix atoms. Therefore, an overlap of atoms may occur and impact the contrast in the STEM images. For the coarse TiN particles with diameter >10 nm (Fig. 22c), a possible NaCl atomic structure was observed, which agrees with a previous report that indicated Ti(N,C,O) precipitates in 14YWT may have a NaCl structure [14]. However, the distinct structure was observed in the bubble (B) region, but not the particle (P) region. The overlap of particles and cavities, which reduces the number of matrix atoms in the analyzed column height, could aid the imaging of the atomic structure of particles. Fig. 22d shows a few bubbles attached to a grain boundary. The atomic structure on the left (L) and right (R) regions are obviously different. In order to minimize the matrix atom distribution, a thinner TEM sample or conducting heat treatment to coarsen the bubbles or nanoparticles (as reported by Stan et al. [40]) would be valuable to visualize the atomic structure of the nanoparticles.

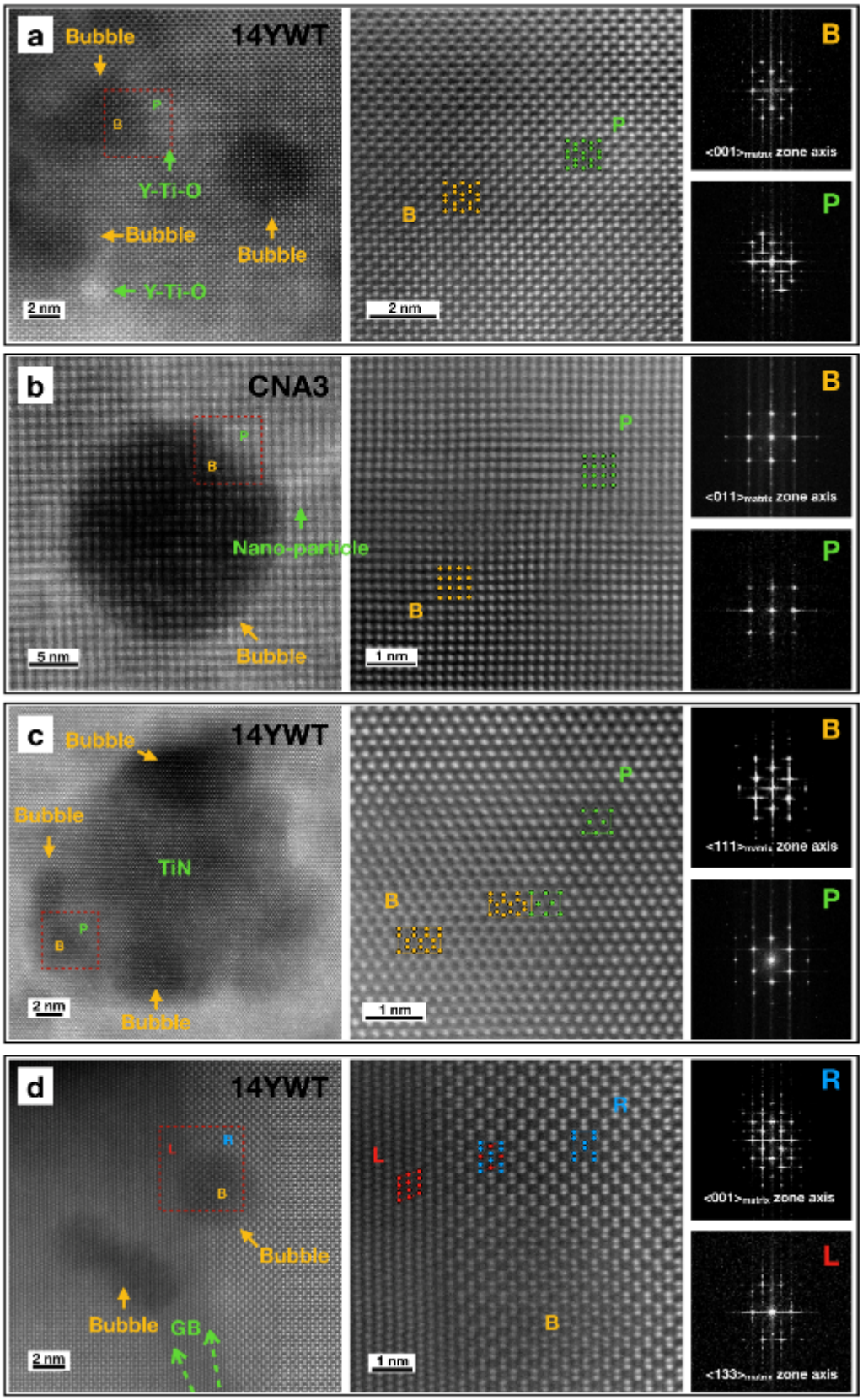
a
Bubble
14YWT
P
B
Y-Ti-O
Bubble
Bubble
Y-Ti-O
2 nm
2 nm
P
B
B
<001>matrix zone axis
P
b
CNA3
P
B
Nano-particle
Bubble
5 nm
1 nm
P
B
B
<011>matrix zone axis
P
c
Bubble
14YWT
Bubble
TiN
P
B
2 nm
Bubble
1 nm
P
B
B
<111>matrix zone axis
P
d
14YWT
L
R
B
Bubble
Bubble
GB
2 nm
1 nm
R
L
B
R
<001>matrix zone axis
L
<133>matrix zone axis

Fig. 22. Atomic resolution STEM-HAADF images of nanoparticles (a-c) or grain boundary (d) and associated helium bubbles in 14YWT and CNA3 nanostructured alloys *ex-situ* irradiated at 700°C. (a) Y-Ti-O, viewed along the <001> Fe-Cr matrix zone axis; (b) (Ti, Ta, W, V)C particle, viewed along the <011> Fe-Cr matrix zone axis; (c) Ti-N, viewed along the <111> Fe-Cr zone axis; and (d) grain boundary, viewed along the <133>(L)/<001>(R) Fe-Cr matrix zone axis. The corresponding FFT patterns of the labeled area are on the right of each figure. (B: He bubble, P: nanoparticle, L: left-grain, R: right-grain)

Conclusions

Cavity formation was examined by TEM and STEM in bulk He-irradiated and in-situ He-irradiated ferritic alloys containing different nanoparticle densities: Fe-9/10Cr (without nano-particles), CNA3 (intermediate), and 14YWT (highest nanoparticle density). The observed bubble number densities and the nanoparticle density in the two nanostructured materials were comparable and a ~1:1 relationship of bubbles attached to nanoparticles was typically observed, suggesting that the nanoparticles were effective in trapping He. The results indicate that very high He concentrations (up to ~10,000 appm) can be well managed in nanostructured alloys with a high density of nanoparticles (10^{22}-10^{24} m^{-3}) by sequestering the helium into smaller bubbles (leading to a lower volume swelling compared to conventional alloys) and to suppress He diffusion to the grain boundaries. Based on the experimental findings the main conclusions are:

(i) In agreement with previous studies, the bubble size was observed to increase with increasing irradiation temperature, while the bubble density decreased with increasing temperature for all three alloy systems.

(ii) At all temperatures, the cavity density in the He implanted materials was generally in the order of Fe-9/10Cr < CNA3 < 14YWT, which directly corresponds to the nanoparticle density, whereas the cavity size showed the opposite order.

(iii) The effective activation energy of Fe-9/10Cr model alloys (without nano-particle) exhibited a weak dependence on temperature below 600°C and a stronger temperature dependence above 600°C. However, the discrepancy of activation energy at high and low temperatures was not significant in the CAN3 and 14YWT nanostructured alloys.

(iv) Comparing the 900 °C post-annealed TEM images with the 900 °C direct-hot-implanted results, the bubble size was only slightly larger in the annealed 14YWT and CNA3 samples, while the cavity radius of Fe-10Cr grew rapidly in the 900°C direct-implanted sample. In addition, the most severe grain boundary cracking was observed in the 900°C direct-implanted Fe-10Cr, which is possibly affected by alpha-gamma phase transition.

(v)14YWT alloy sequesters the helium into smaller bubbles more effectively than the other alloys. This may be attributed to the much higher sink strength associated with the nanoclusters in the 14YWT alloy, or the difference of the He trapping ability (binding energy) between oxides and MX precipitates.

Acknowledgments

The authors are thankful for the IVEM tandem facility support from Argonne National Laboratory, and the ion accelerator support from National Tsing Hua University. The authors would also like to acknowledge funding from the State of Tennessee and Tennessee Higher Education Commission (THEC) through their support of the Center for Materials Processing. We thank Drs. Arunodaya Bhattacharya, Roger Stoller, Brian Wirth, William Weber, and Haixuan Xu for their insightful comments and suggestions.

Funding: This work was supported by the U.S. Department of Energy, Office of Nuclear Energy under DOE Idaho Operations Office Contract DE-AC07- 051D14517 as part of a Nuclear Science User Facilities experiment. This research was also sponsored by the Office of Fusion Energy Sciences, U.S. Department of Energy under grant # DE-SC0006661 with the University of Tennessee (YRL and SJZ). The fabrication of the Fe-Cr binary alloys has been carried out within the framework of the EUROfusion Consortium and has received funding from the Euratom research and training program 2019–2020 under Grant Agreement No. 633053.

Declarations of Interest:

None.

References

[1] J. Knaster, A. Moeslang, T. Muroga, Materials research for fusion, Nature Physics 12(5) (2016) 424-434.

[2] Y. Dai, G.R. Odette, T. Yamamoto, 1.06 - The Effects of Helium in Irradiated Structural Alloys, in: R.J.M. Konings (Ed.), Comprehensive Nuclear Materials, Elsevier, Oxford, 2012, pp. 141-193.

[3] T. Yamamoto, G.R. Odette, H. Kishimoto, J.-W. Rensman, P. Miao, On the effects of irradiation and helium on the yield stress changes and hardening and non-hardening embrittlement of ~8Cr tempered martensitic steels: Compilation and analysis of existing data, Journal of Nuclear Materials 356(1) (2006) 27-49.

[4] N.H. Packan, K. Farrell, Simulation of first wall damage: Effects of the method of gas implantation, Journal of Nuclear Materials 85-86 (1979) 677-681.

[5] A. Bhattacharya, S.J. Zinkle, 1.12 - Cavity Swelling in Irradiated Materials, in: R.J.M. Konings, R.E. Stoller (Eds.), Comprehensive Nuclear Materials (Second Edition), Elsevier, Oxford, 2020, pp. 406-455.

[6] E.E. Bloom, F.W. Wiffen, The effects of large concentrations of helium on the mechanical properties of neutron-irradiated stainless steel, Journal of Nuclear Materials 58(2) (1975) 171-184.

[7] S.J. Zinkle, L.L. Snead, Designing Radiation Resistance in Materials for Fusion Energy, Annual Review of Materials Research 44(1) (2014) 241-267.

[8] G.R. Odette, M.J. Alinger, B.D. Wirth, Recent Developments in Irradiation-Resistant Steels, Annual Review of Materials Research 38(1) (2008) 471-503.

[9] L. Tan, L.L. Snead, Y. Katoh, Development of new generation reduced activation ferritic-martensitic steels for advanced fusion reactors, Journal of Nuclear Materials 478 (2016) 42-49.

[10] C.P. Massey, S.N. Dryepondt, P.D. Edmondson, M.G. Frith, K.C. Littrell, A. Kini, B. Gault, K.A. Terrani, S.J. Zinkle, Multiscale investigations of nanoprecipitate nucleation, growth, and coarsening in annealed low-Cr oxide dispersion strengthened FeCrAl powder, Acta Materialia 166 (2019) 1-17.

[11] R. Lindau, A. Möslang, M. Rieth, M. Klimiankou, E. Materna-Morris, A. Alamo, A.A.F. Tavassoli, C. Cayron, A.M. Lancha, P. Fernandez, N. Baluc, R. Schäublin, E. Diegele, G. Filacchioni, J.W. Rensman, B.v.d. Schaaf, E. Lucon, W. Dietz, Present development status of EUROFER and ODS-EUROFER for application in blanket concepts, Fusion Engineering and Design 75-79 (2005) 989-996.

[12] M.K. Miller, K.F. Russell, D.T. Hoelzer, Characterization of precipitates in MA/ODS ferritic alloys, Journal of Nuclear Materials 351(1) (2006) 261-268.

[13] E. Aydogan, S.A. Maloy, O. Anderoglu, C. Sun, J.G. Gigax, L. Shao, F.A. Garner, I.E. Anderson, J.J. Lewandowski, Effect of tube processing methods on microstructure, mechanical properties and irradiation response of 14YWT nanostructured ferritic alloys, Acta Materialia 134 (2017) 116-127.

[14] P.D. Edmondson, C.M. Parish, Y. Zhang, A. Hallén, M.K. Miller, Helium bubble distributions in a nanostructured ferritic alloy, Journal of Nuclear Materials 434(1) (2013) 210-216.

[15] P.D. Edmondson, C.M. Parish, Q. Li, M.K. Miller, Thermal stability of nanoscale helium bubbles in a 14YWT nanostructured ferritic alloy, Journal of Nuclear Materials 445(1) (2014) 84-90.

[16] C.M. Parish, K.A. Unocic, L. Tan, S.J. Zinkle, S. Kondo, L.L. Snead, D.T. Hoelzer, Y. Katoh, Helium sequestration at nanoparticle-matrix interfaces in helium + heavy ion irradiated nanostructured ferritic alloys, Journal of Nuclear Materials 483 (2017) 21-34.

[17] T. Yamamoto, Y. Wu, G. Robert Odette, K. Yabuuchi, S. Kondo, A. Kimura, A dual ion irradiation study of helium–dpa interactions on cavity evolution in tempered martensitic steels and nanostructured ferritic alloys, Journal of Nuclear Materials 449(1) (2014) 190-199.

[18] G.R. Odette, Recent Progress in Developing and Qualifying Nanostructured Ferritic Alloys for Advanced Fission and Fusion Applications, JOM 66(12) (2014) 2427-2441.

[19] A. Kohyama, G. Ayrault, N. Igata, Microstructural evolution in dual-ion irradiated 316ss under various helium injection schedules, Journal of Nuclear Materials 122(1) (1984) 224-229.

[20] K. Farrell, Experimental effects of helium on cavity formation during irradiation—a review, Radiation Effects 53(3-4) (1980) 175-194.

[21] B.N. Singh, H. Trinkaus, An analysis of the bubble formation behaviour under different experimental conditions, Journal of Nuclear Materials 186(2) (1992) 153-165.

[22] K. Ono, K. Arakawa, K. Hojou, Formation and migration of helium bubbles in Fe and Fe–9Cr ferritic alloy, Journal of Nuclear Materials 307-311 (2002) 1507-1512.

[23] P. Dauben, R.P. Wahi, H. Wollenberger, Bubble nucleation and growth in an Fe-12 at% Cr ferritic alloy under He+ implantation and Fe+ irradiation, Journal of Nuclear Materials 141-143 (1986) 723-726.

[24] Z. Yan, T. Yang, Y. Lin, Y. Lu, Y. Su, S.J. Zinkle, Y. Wang, Effects of temperature on helium bubble behaviour in Fe–9Cr alloy, Journal of Nuclear Materials 532 (2020) 152045.

[25] D. Brimbal, E. Meslin, J. Henry, B. Décamps, A. Barbu, He and Cr effects on radiation damage formation in ion-irradiated pure iron and Fe–5.40wt.% Cr: A transmission electron microscopy study, Acta Materialia 61(13) (2013) 4757-4764.

[26] Y.-R. Lin, A. Bhattacharya, D. Chen, J.-j. Kai, J. Henry, S. Zinkle, Temperature-Dependent Cavity Swelling in Dual-Ion Irradiated Fe and Fe-Cr Ferritic Alloys, Acta Materialia 207 (2021) 116660.

[27] D.B. Williams, C.B. Carter, Electron Energy-Loss Spectrometers and Filters, in: D.B. Williams, C.B. Carter (Eds.), Transmission Electron Microscopy: A Textbook for Materials Science, Springer US, Boston, MA, 2009, pp. 679-698.

[28] Y.-R. Lin, L.-G. Chen, C.-Y. Hsieh, A. Hu, S.-C. Lo, F.-R. Chen, J.-J. Kai, Atomic structure of nano voids in irradiated 3C-SiC, Journal of Nuclear Materials 498 (2018) 71-75.

[29] Y.R. Lin, L.G. Chen, C.Y. Hsieh, M.T. Chang, K.Y. Fung, A. Hu, S.C. Lo, F.R. Chen, J.J. Kai, Atomic Configuration of Point Defect Clusters in Ion-Irradiated Silicon Carbide, Scientific Reports 7(1) (2017) 14635.

[30] S. Van Aert, K.J. Batenburg, M.D. Rossell, R. Erni, G. Van Tendeloo, Three-dimensional atomic imaging of crystalline nanoparticles, Nature 470(7334) (2011) 374-377.

[31] H. Okamoto, M.E. Schlesinger, E.M. Mueller, Hf (Hafnium) Binary Alloy Phase Diagrams, Alloy Phase Diagrams, ASM International2016, p. 0.

[32] S.J. Zinkle, G.S. Was, Materials challenges in nuclear energy, Acta Materialia 61(3) (2013) 735-758.

[33] K. Ono, K. Arakawa, H. Shibasaki, H. Kurata, I. Nakamichi, N. Yoshida, Release of helium from irradiation damage in Fe–9Cr ferritic alloy, Journal of Nuclear Materials 329-333 (2004) 933-937.

[34] N.L. Peterson, Grain-boundary diffusion in metals, International Metals Reviews 28(1) (1983) 65-91.

[35] P.L. Lane, P.J. Goodhew, Helium bubble nucleation at grain boundaries, Philosophical Magazine A 48(6) (1983) 965-986.

[36] C. Lu, Z. Lu, X. Wang, R. Xie, Z. Li, M. Higgins, C. Liu, F. Gao, L. Wang, Enhanced Radiation-tolerant Oxide Dispersion Strengthened Steel and its Microstructure Evolution under Helium-implantation and Heavy-ion Irradiation, Scientific Reports 7(1) (2017) 40343.

[37] D. Brimbal, L. Beck, O. Troeber, E. Gaganidze, P. Trocellier, J. Aktaa, R. Lindau, Microstructural characterization of Eurofer-97 and Eurofer-ODS steels before and after multi-beam ion irradiations at JANNUS Saclay facility, Journal of Nuclear Materials 465 (2015) 236-244.

[38] T. Yamamoto, G.R. Odette, P. Miao, D.T. Hoelzer, J. Bentley, N. Hashimoto, H. Tanigawa, R.J. Kurtz, The transport and fate of helium in nanostructured ferritic alloys at fusion relevant He/dpa ratios and dpa rates, Journal of Nuclear Materials 367-370 (2007) 399-410.

[39] L.K. Mansur, Void Swelling in Metals and Alloys Under Irradiation: An Assessment of the Theory, Nuclear Technology 40(1) (1978) 5-34.

[40] T. Stan, Y. Wu, J. Ciston, T. Yamamoto, G.R. Odette, Characterization of polyhedral nano-oxides and helium bubbles in an annealed nanostructured ferritic alloy, Acta Materialia 183 (2020) 484-492.